Check for updates

Received: 20 March 2025 | Revised: 4 July 2025 | Accepted: 17 July 2025

DOI: 10.1002/dep2.70031

The Depositional Record
Open Access
A journal of the International Association of Sedimentologists
WILEY

ORIGINAL ARTICLE

A continuous 500-year sediment record of inundation by local and distant tsunamis in South-Central Chile (40.1°S)

Jasper Moernaut[1] | **Evelien Boes**[2] | **Daniel Melnick**[3] | **Matías Carvajal**[4] | **Markus Niederstätter**[1] | **Sabine Schmidt**[5] | **Diego Aedo**[6] | **Mario Pino**[3] | **Marc De Batist**[2]

[1]Institute of Geology, University of Innsbruck, Innsbruck, Austria

[2]Renard Centre of Marine Geology (RCMG), Department of Geology, Ghent University, Ghent, Belgium

[3]Instituto de Ciencias de la Tierra, Universidad Austral de Chile, Valdivia, Chile

[4]Instituto de Geografía, Pontificia Universidad Católica de Valparaíso, Valparaíso, Chile

[5]Environnements et Paléoenvironnements Océaniques et Continentaux, University of Bordeaux, Pessac Cedex, France

[6]Departamento Ciencias de la Tierra, Facultad de Ciencias Químicas, Universidad de Concepción, Concepción, Chile

Correspondence
Jasper Moernaut, Institute of Geology, University of Innsbruck, Innrain 52, Innsbruck 6020, Austria.
Email: jasper.moernaut@uibk.ac.at

Funding information
Fondo Nacional de Desarrollo Científico y Tecnológico, Grant/Award Number: 1150346 and 1231735; Fonds Wetenschappelijk Onderzoek; Austrian Science Fund, Grant/Award Number: 10.55776/P30285

Abstract

Chile's west coast is frequently struck by megathrust earthquakes and tsunamis, as illustrated by the CE 2010 Maule (M_w 8.8) and CE 1960 Valdivia (M_w 9.5) events. Despite numerous palaeoseismic and palaeotsunami studies, uncertainties remain regarding the rupture extent and tsunamigenic potential of M_w 8–9 earthquakes. This study examines the sedimentary record of Laguna Gemela West, a coastal lake at 5–6 m a.s.l. and of 17.5 m depth. It is separated from the Pacific by a 400 m long channel bordered by northward-propagating dunes and controlled by Pleistocene sandstones forming a knickpoint in the channel profile. Multiple sedimentary proxies (e.g. grain-size, X-CT, XRF scanning) identified five distinct sand-enriched layers, interpreted as tsunami deposits. Age-depth modelling (based on 137Cs and 14C) allowed linking these deposits to the CE 2010, 1960, 1837, 1737 and 1575 megathrust earthquakes. While historical records confirm significant tsunamis in CE 2010, 1960, 1837 and 1575, no reports exist for a CE 1737 tsunami. However, a potential tsunami deposit and evidence for subsidence were found at the nearby Chaihuín site, albeit with large dating uncertainty (CE 1600–1820). The more precise age for a sand layer at Laguna Gemela West (CE 1672–1746) supports the occurrence of a local tsunami in CE 1737. Additionally, deposits linked to the CE 1837 and 2010 events suggest tsunamis can impact sites >100 km adjacent to megathrust ruptures. A second pulse in the uppermost sand layer may reflect the CE 2011 Japan tsunami, which reached a similar height (~1.6 m a.s.l.) in the nearest tide gauge as the CE 2010 tsunami. Unlike coastal plain sites, which often require coseismic subsidence for deposit preservation, coastal lakes can capture a more complete tsunami history. This study highlights their complementary role in palaeotsunami research, providing insights in local, regional and transoceanic tsunami events.

Jasper Moernaut and Evelien Boes share equal first authorship.

This is an open access article under the terms of the Creative Commons Attribution License, which permits use, distribution and reproduction in any medium, provided the original work is properly cited.
© 2025 The Author(s). *The Depositional Record* published by John Wiley & Sons Ltd on behalf of International Association of Sedimentologists.

KEYWORDS
coastal lake, limnogeology, Megathrust earthquake, tsunami deposit

1 | INTRODUCTION

Megathrust faults at the plate interface of subduction zones are capable of producing some of the largest earthquakes and most extensive tsunamis on Earth. Because the timescales of their recurrence patterns commonly exceed those of instrumental and historical records, current seismic and tsunami hazard assessments may rely on catalogues that are deficient. Despite dense seismicity monitoring, space geodetic surveys and a recent 'boom' in palaeoseismic and palaeotsunami research at subduction zones, our understanding of megathrust earthquake recurrence patterns is far from complete (Philibosian & Meltzner, 2020). As tsunamis generated by megathrust earthquakes typically have a larger death toll than those produced by their seismic ground motion, it is vital to better constrain the variability and tsunamigenic potential of megathrust ruptures.

The South-Central Chilean subduction zone is notorious for having generated the largest instrumentally recorded earthquake in CE 1960, with an M_w of 9.2–9.6 (Ho et al., 2019). Numerous studies in the CE 1960 rupture area focused on extracting long sedimentary records of past seismic shaking, coastal elevation changes and tsunami inundation, revealing a quasi-periodic recurrence interval of giant (M_w 9+) earthquakes associated with long (600–1000 km) ruptures spanning the full downdip megathrust width (150–200 km) (Cisternas et al., 2005; Moernaut et al., 2018; Wils et al., 2020). These cycles of giant earthquakes are interspersed with smaller, yet still great earthquakes (M_w 8–9) characterised by shorter ruptures that may only partially span the downdip megathrust width, resulting in a highly variable tsunamigenic character (Cisternas et al., 2017; Hocking et al., 2021; Lomnitz, 2004; Moernaut et al., 2014). In historical times, the tsunami produced by the CE 1837 earthquake (Figure 1A; see Section 2.1) took human lives as far as Hawaii and caused damage in Japan, whereas for the CE 1737 earthquake, no tsunami was reported in Chile or elsewhere (Cisternas et al., 2017). These observations have been explained by a rupture extending offshore in CE 1837 but limited to beneath land in CE 1737 (Cisternas et al., 2018). This interpretation, based on historical records alone, was recently challenged by a coastal marsh record (Hocking et al., 2021) that shows sedimentary and palaeoecological evidence for tsunami inundation and coseismic subsidence dated to CE 1600–1820, suggesting that a local tsunami may have indeed occurred in CE 1737. However, due to the plateaus in the ^{14}C calibration curve, it is difficult to robustly assign a coastal marsh deposit to the CE 1737 event through ^{14}C dating of the bounding sedimentary units. Therefore, the existence of a CE 1737 tsunami remains a topic of debate and it is thus unclear how frequently the study area is subjected to tsunami inundation. Moreover, at many coastal sites, coseismic subsidence is required to generate sufficient accommodation space for tsunami deposits to be preserved in the sedimentary record (e.g. Clark et al., 2019). One exception would be coastal marshes in a ridge-and-swale topography, which have yielded excellent palaeotsunami records, for example, in Indonesia or Thailand (Jankaew et al., 2008; Monecke et al., 2008). In South-Central Chile, the published coastal plain/marsh palaeotsunami records were mostly obtained in other settings and therefore may be incomplete for tsunamis that were generated at adjacent megathrust fault sections or for tele-tsunamis.

Coastal lakes that are several metres deep provide a potential solution for this problem concerning dating and preservation, because abundant accommodation space allows for continuous and stable sedimentation between the inundation events (Avşar, 2019; Jackson et al., 2014; Kelsey et al., 2005; Kempf et al., 2017; Sabatier et al., 2022; Sawai et al., 2008). Consequently, reconstructed accumulation histories tied to (i) ^{14}C ages older than the mentioned calibration plateau and (ii) to $^{137}Cs/^{210}Pb$-based age information for the last 150 years could provide better age control. Despite a good preservation potential for tsunami deposits, the sedimentary record of coastal lakes and lagoons has not yet been exploited to the same extent as the more conventionally studied coastal plains and marshes. In South-Central Chile, the few studied tsunami records in coastal lakes (Figure 1) are located much further south (~280 km; Lake Cucao and Lake Huelde; Kempf et al., 2017, 2020) or are very fragmented prior to CE 1960 (Lake Budi; Wallner, 2007).

Here, we use a combined geophysical, sedimentological and geochemical approach to study the last 500 years of the sedimentary record in a small coastal lake in the northern half of the CE 1960 rupture zone in South-Central Chile (40.1°S). We specifically evaluate whether historical megathrust earthquakes produced a tsunami deposit in the lake and interpret these findings with regard to the local geomorphology, sea-level data and the nearby Chaihuín coastal marsh record. We further discuss the implications of this coastal lake record for subduction zone palaeoseismology in Chile.

20554877, 2025, 5, Downloaded from https://onlinelibrary.wiley.com/doi/10.1002/dep2.70031, Wiley Online Library on [16/12/2025]. See the Terms and Conditions (https://onlinelibrary.wiley.com/terms-and-conditions) on Wiley Online Library for rules of use; OA articles are governed by the applicable Creative Commons License

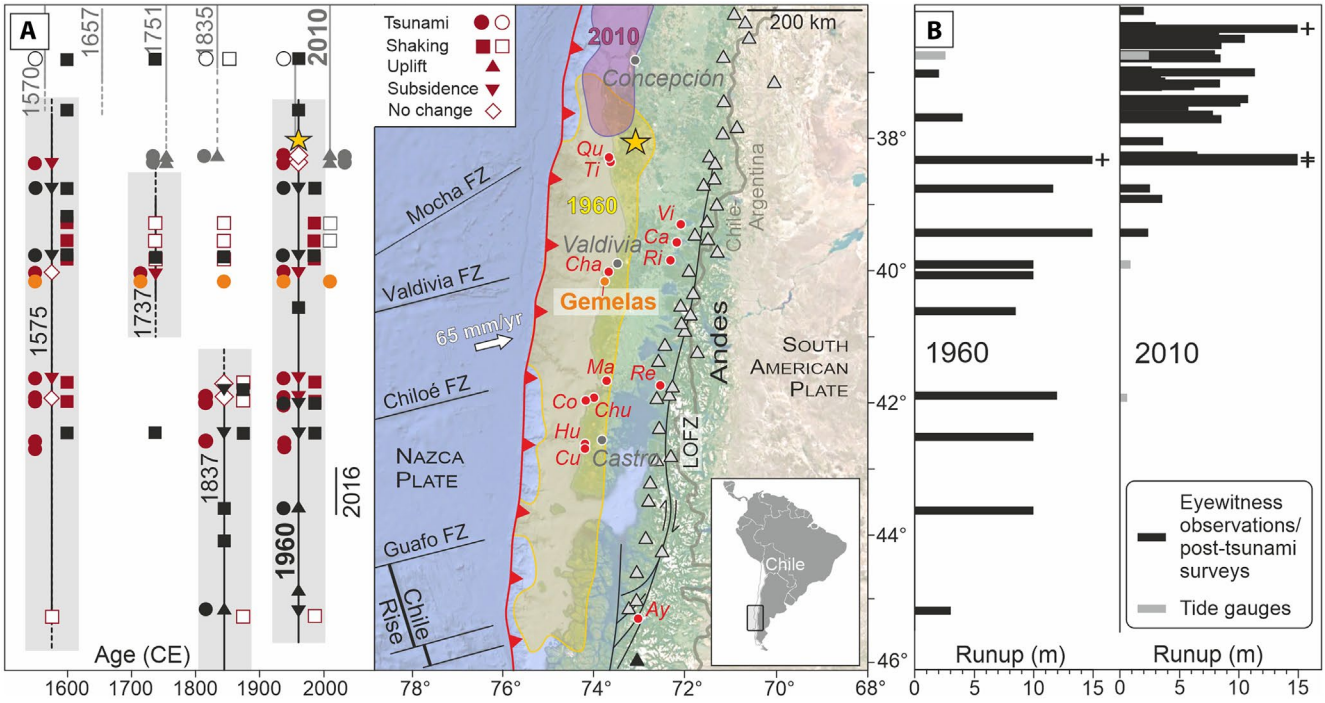

FIGURE 1 (A) Tectonic setting of the study area (~30–46°S) in South-Central Chile with location of Laguna Gemela West, and palaeoseismic and palaeotsunami sites in the region that cover at least the last 500 years (red dots). Qu: Quidico; Ti: Tirúa; Vi: Villarrica; Ca: Calafquén; Ri: Riñihue; Cha: Chaihuín; Ma: Maullín; Re: Reloncavi; Chu: Chucalén; Co: Cocotue; Hu: Huelde; Cu: Cucao; Ay: Aysén. Triangles: Active volcanoes. FZ: Oceanic Fracture Zone. LOFZ: Liquiñe-Ofqui Fault Zone. The rupture area of the CE 1960 (M_w 9.5; yellow) and CE 2010 (M_w 8.8; purple) earthquakes are indicated. Epicentre of the CE 1960 earthquake (yellow star). Left: Type of sedimentary evidence (in red) and historical evidence (in black) at each site (see legend). Empty squares and circles relate to less intense shaking or smaller tsunami size, respectively. For events north of 39°S, we only show sedimentary evidence (in grey). Estimated extent of historical megathrust earthquake ruptures (after Cisternas et al., 2017; Hocking et al., 2021) as full lines and grey rectangles. Dashed lines indicate large uncertainty. (B) Run-up heights of tsunami waves following the CE 1960 earthquake (NOAA database) and CE 2010 earthquake (Fritz et al., 2011), based on eyewitness observations and post-tsunami surveys.

2 | SETTING

2.1 | Seismo-tectonic setting, historical earthquakes and tsunamis

The seismo-tectonic setting of South-Central Chile is dominated by the subduction of the Nazca plate beneath the South America Plate with a convergence rate of ~6.5 mm/year (Jarrin et al., 2022). In CE 2010, the subduction megathrust fault ruptured over about 500 km between 33.7°S and 38.5°S with slip values of 10–15 m (Zhang et al., 2021), resulting in a M_w 8.8 earthquake (Figure 1). Its tsunami was destructive in the rupture region with average run-up heights of 5–10 m and local peaks exceeding 20 m (Fritz et al., 2011). This event was preceded by great historical events in CE 1835, 1751, 1657 and 1570, plus many other smaller earthquakes. From sparse historical documents, it is suggested that the CE 1751 event was comparable in size and tsunamigenesis with the CE 2010 earthquake (Udías et al., 2012), whereas the CE 1835 event may not have extended as far north (~35.5°S) and south (~37°S) (Ruiz & Madariaga, 2018). This is consistent with the coastal river plain records in Tirúa (38.3°S; Figure 1A) where coastal uplift in CE 1751 and CE 2010 was inferred, but not for the CE 1835 event (Ely et al., 2014). However, the slightly northern Quidico site (38.1°S) does show a tsunami deposit and coseismic uplift in CE 1835 (Dura et al., 2017), suggesting that the CE 1835 rupture terminated somewhere in this area.

Just south of the CE 2010 rupture, the CE 1960 earthquake (M_w 9.2–9.6) ruptured the megathrust for ~1000 km with average slip values between 15 m and 25 m, and high slip patches of up to 40 m (Ho et al., 2019; Moreno et al., 2009). These giant rupture dimensions triggered an extensive trans-Pacific tsunami that killed 61 people in Hawaii and 139 in Japan. In Chile, a large tsunami was reported with average run-up heights of 10 m and local extremes greater than 20 m (Figure 1B; NOAA; National Geophysical Data Center/World Data Service, 2025, https://www.ngdc.noaa.gov/hazel/view/hazards/tsunami/related-runups/1902). Associated tsunami deposits in Chile were recorded in a number of coastal river plains, marshes and lakes (León et al., 2023). Historical documents and

20554877, 2025, 5, Downloaded from https://onlinelibrary.wiley.com/doi/10.1002/dep2.70031, Wiley Online Library on [16/12/2025]. See the Terms and Conditions (https://onlinelibrary.wiley.com/terms-and-conditions) on Wiley Online Library for rules of use; OA articles are governed by the applicable Creative Commons License

sedimentary records attest that a seemingly similar event occurred in CE 1575 (Cisternas et al., 2005, 2018; Garrett et al., 2015; Moernaut et al., 2014; Wils et al., 2020).

Two historical events greater than M_w 8 occurred in CE 1837 and CE 1737, and each ruptured only a part of the CE 1960 rupture area (Lomnitz, 2004). These are inferred to have occurred in the southern half and northern third of the CE 1960 zone, respectively (Figure 1) (Cisternas et al., 2017). The CE 1837 earthquake and tsunami are well documented in historical reports, and comparative analysis of tsunami heights in Japan suggests a M_w 9¼ (Abe, 1979). Only two coastal records in South-Central Chile (Lago Huelde: Kempf et al., 2017; Cocotué site: Cisternas et al., 2018) show sedimentary evidence for this tsunami. Coseismic coastal elevation changes were mainly documented in remote locations near the southern limit of the CE 1960 zone (Figure 1; Cisternas et al., 2017). In contrast, historical documentation for the CE 1737 event is rather scarce and no tsunami was reported, but this could also relate to limitations in historical recording, as uprisings by indigenous communities restricted the number of colonial outposts in the region. One coastal site (Chaihuín site) shows potential traces for tsunami and coseismic subsidence in CE 1737 (Hocking et al., 2021). For both the CE 1837 and CE 1737 events, seismo-turbidites in more inland lakes between 39.2°S and 39.8°S (i.e. lakes Villarrica, Calafquén, Riñihue; Figure 1A) attest that shaking was significant with a seismic intensity of ~VI½, but clearly more modest than in CE 1960 and CE 1575 when a seismic intensity of ~VII½ struck the region (Moernaut et al., 2014). Such a reduced seismic intensity supports the hypothesis of a shorter rupture in CE 1737 at the latitude of the studied inland lakes and a more southern and longer rupture in CE 1837 which did not reach that latitude (Figure 1). This is because a hypothetical long high-slip rupture near the lakes would have generated stronger and prolonged shaking and thus large seismo-turbidites across the lakes, such as those from the CE 1960 and CE 1575 earthquakes (Moernaut et al., 2014).

2.2 | Local setting: Laguna Gemela West

We investigated Laguna Gemela West (40.07°S, 73.65°W), the western and most accessible lake of the so-called twin lakes (Lagunas Gemelas) near the remote Colún Beach at the Pacific Ocean (Figures 2 and 3). Laguna Gemela East has not been studied because of poor accessibility. The lake surface of Gemela West extends over 0.28 km^2 and is located at ~5–6 m a.s.l. (m above sea level) (see Section 4.1; Lagos, 2008; Palacios, 2008). The lake has a maximum water depth of ~18 m. In March 2008, it consisted of fresh water with a low conductivity (~100–110 µs/cm, Palacios, 2008). Spring tides reach approximately 1 m a.s.l. in the nearby tide gauge station of Corral, according to data from the IOC Sea Level Monitoring Facility (Flanders Marine Institute (VLIZ), 2024; discussion Section 5.2). The lake basin occupies a former river valley, which follows the structural lineaments in the region, suggesting a strong tectonic control on valley formation. As the lake bottom is below current sea level and outside the glacier limits of the last glaciations, valley formation is inferred to result from fluvial incision during glacial periods (Lagos, 2008) when eustatic sea level was several 10s of metres lower, down to ~−120 m a.s.l. during the last glacial maximum. The lake outflow reaches the ocean via a 400 m long winding channel incised in Pleistocene sedimentary rock formations, locally known as 'Cancagua' (Illies, 1970; SERNAGEOMIN, 2003; Vega et al., 2018). The channel is bordered to the south by dune sand that covers the 20–30 m high bedrock (Figures 2 and 3). The lake is fed by intense rainfall with an annual average of ~2077 mm at Punta Galeras (~8 km NNW of the lake; Di Castri & Hajek, 1976) and surface run-off from a rather small catchment of 1.7 km^2 (Lagos, 2008). Its surroundings are completely covered with evergreen Valdivian temperate forest. Intense forestry activities (including native forest burning and replacement by *Eucalyptus* trees) took place in the 1990s and early 2000s, affecting the outer parts of the lake catchment, whereas native forests at the lake shore remained intact. Since 2003, the entire region became protected as the Valdivian Coastal Reserve, the largest protected area in the Chilean Coastal Range and administered by The Nature Conservancy (https://www.nature.org/en-us/).

3 | MATERIALS AND METHODS

3.1 | UAV photogrammetry and dGPS points

We surveyed the outlet of the Laguna Gemela West using a Matrice 200 DJI drone equipped with a Xenmuse camera and a Trimble R8S RTK GNSS instrument. With the drone, we acquired 469 aerial images in crossline survey mode used to construct a point cloud using Pix4D v3 photogrammetric software. The RTK GNSS device was used to survey static ground control points as well as a longitudinal profile of the outlet stream in kinematic mode at a 1 Hz sampling rate. Referencing the elevation to mean sea level using tidal levels showed difficulties due to the large run-up of wind waves, and therefore, we used the wet–dry line, which is clearly distinguishable in the orthomosaic constructed from the drone photos and has been commonly used as representative of mean

20554877, 2025, 5, Downloaded from https://onlinelibrary.wiley.com/doi/10.1002/dep2.70031, Wiley Online Library on [16/12/2025]. See the Terms and Conditions (https://onlinelibrary.wiley.com/terms-and-conditions) on Wiley Online Library for rules of use; OA articles are governed by the applicable Creative Commons License

FIGURE 2 Local setting and terrestrial samples (January 2016 field survey). Upper left: Satellite image of Lagunas Gemelas and its environs (GoogleEarth, January 2011). South of Gemela West, a 2 km long and 700 m wide stretch of large coastal sand dunes reaches up to the estuary of Río Colún. A 400 m long, winding outlet connects Gemela West with Playa Colún and the Pacific Ocean. The outlet cuts through Pleistocene sandstone formations (Cancagua beds). Locations of collected surface samples are marked with coloured circles on the map and photographs. White, numbered balloons show the location and direction of photographs. Photographs: (1) Eastward view on Laguna Gemela West; (2) low vegetation at mouth of outlet at the lake shore; (3) beach view towards the south; (4) Playa Colún with massive dunes; (5) narrow outflow channel eroded in sandstone; (6) view on 30 m high dunes that shield the outlet; (7) small waterfall of the outflowing creek over the sandstone barrier; (8) shielding sand dunes covering the creek; (9) dry outlet with bleached logs; (10) opening of outlet creek to the beach and ocean, with outcropping, oxidised Cancagua sandstone.

20554877, 2025, 5, Downloaded from https://onlinelibrary.wiley.com/doi/10.1002/dep2.70031, Wiley Online Library on [16/12/2025]. See the Terms and Conditions (https://onlinelibrary.wiley.com/terms-and-conditions) on Wiley Online Library for rules of use; OA articles are governed by the applicable Creative Commons License

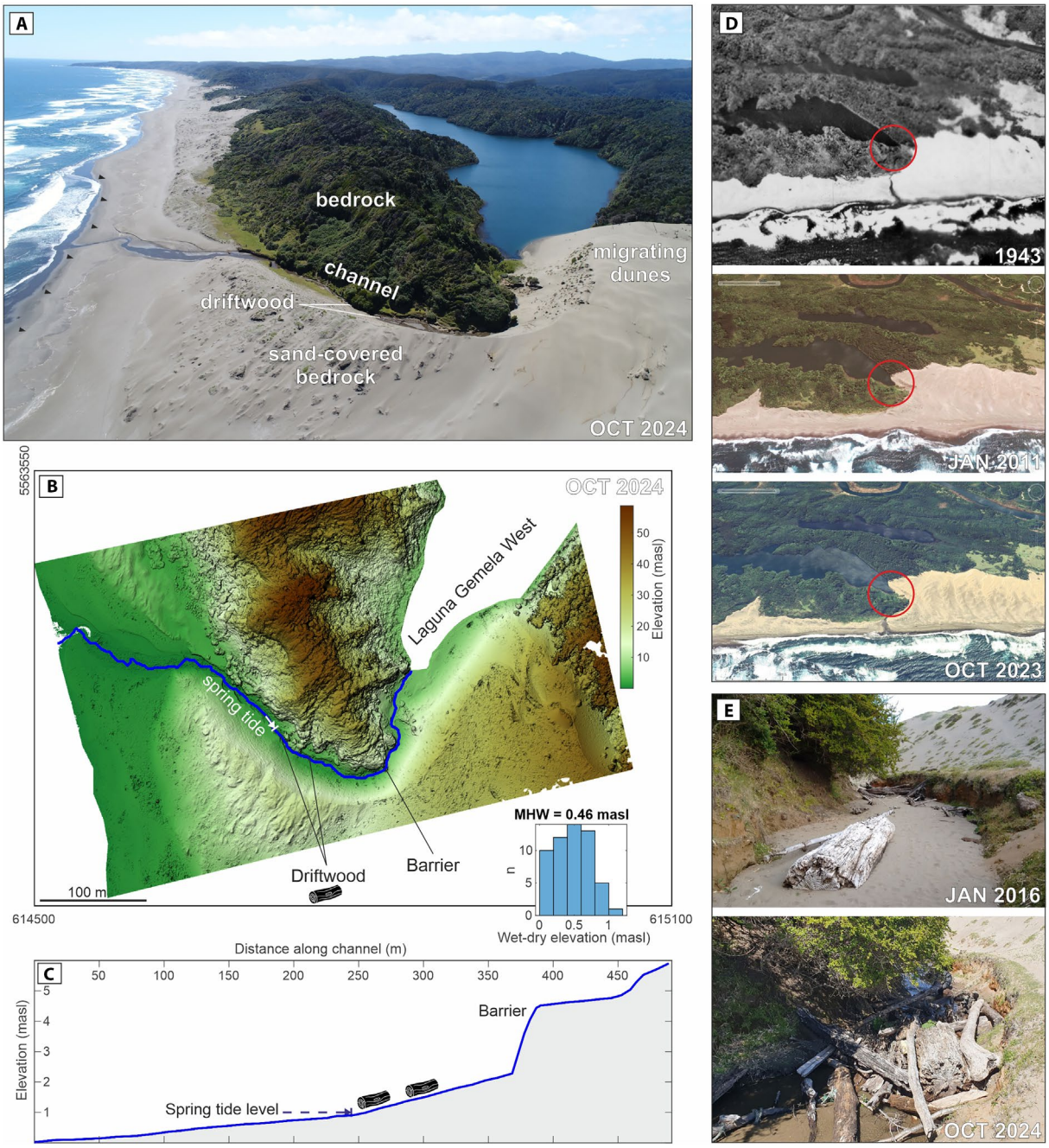

FIGURE 3 Local geomorphology (2024 field survey) and time series of imagery. (A) Oblique UAV (drone) picture showing the main geomorphological features of the study area. Black triangles indicate the wet–dry line. (B) Digital elevation model (20 cm horizontal resolution) based on UAV Photogrammetry. Inset histogram: Measurements of the wet–dry line calibrated to the Mean High Water tidal datum from the TPXO Atlas tidal model (Section 3.1). (C) Elevation profile along the outlet channel based on the calibrated photogrammetric elevation data. Linear interpolation is performed at the barrier as the narrow gorge precluded the acquisition of data from the drone or RTK GNSS. (D) Oblique (East-looking) aerial imagery from the 1943 Trimetrogón flight compared to inclined Google Earth satellite images from January 2011 and October 2023. The area in the red circle indicates dune migration, currently covering vegetation and bedrock at the southern lake shore. (E) Observation of driftwood and human-made debris (tire, fishing wires) halfway the outlet channel. The position of trunks changed between January 2016 and October 2024.

high water tidal datum (Boak & Turner, 2005). We digitised 55 points along the wet–dry line on the orthomosaic and estimated their mean elevation and standard deviation (inset in Figure 3B). We estimated the elevation of the MHW using 20 years of tides calculated using the TPXO Atlas tidal model (Egbert & Erofeeva, 2002) to 0.46 m and referred all the elevation data to mean sea level. We assign the standard deviation of the wet–dry

20554877, 2025, 5, Downloaded from https://onlinelibrary.wiley.com/doi/10.1002/dep2.70031, Wiley Online Library on [16/12/2025]. See the Terms and Conditions (https://onlinelibrary.wiley.com/terms-and-conditions) on Wiley Online Library for rules of use; OA articles are governed by the applicable Creative Commons License

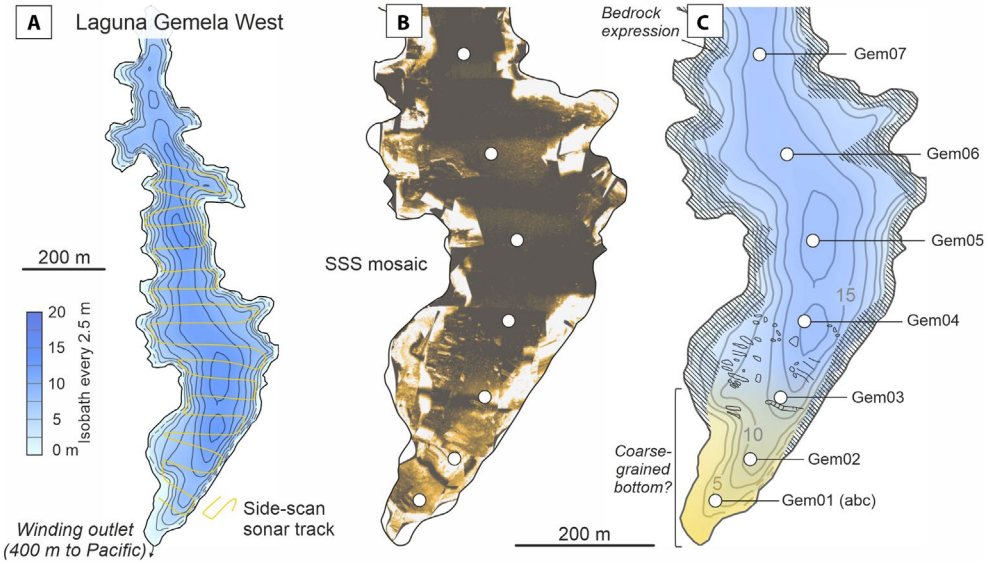

FIGURE 4 (A) Bathymetry of Laguna Gemela West based on side-scan sonar (SSS) mapping (yellow track) and the bathymetric map presented in Palacios (2008). (B) SSS mosaic (black = low intensity of the reflected signal). White dots: Locations of hammer coring sites (Gem01–07). (C) General interpretation of the SSS data indicating outcropping bedrock along the lake basin and a broad zone of potentially coarse sediments at the shallower southern end of the lake.

line elevation (±0.2 m) as the uncertainty of the absolute elevation estimates, neglecting further uncertainties associated with referencing and processing of the photogrammetry data as these are usually at the centimetre level (Lundine, 2018).

A longitudinal channel elevation profile was extracted from the photogrammetric elevation data by tracing the water-filled parts of the channel on the orthomosaic image. Along the knickpoint, the outlet channel is in a narrow gorge covered by trees, and therefore, it was not possible to obtain reliable data neither from the RTK nor from the drone data. At this location, we used linear interpolation between high-quality data points, which may underestimate the real slope gradients at the gorge.

3.2 | Geophysical imaging of the lake bottom

The bottom of Laguna Gemela West was imaged in January 2016 with a side-scan sonar (SSS) Klein 3000 system with a simultaneous dual-frequency (100 and 500 kHz) operation and a swath width of 150 m (Figure 4). Full coverage was achieved by obtaining lines with one swath width of overlap. SonarPro software (Klein Associates) was used for data acquisition and in-field visualisation of acoustic reflectivity, and SonarWizMap software (Chesapeake Technology) for processing and mosaicking. The degree of SSS reflected intensity depends on topography and acoustic hardness of the substrate, allowing detection of lake bottom features. Water depths were extracted along bottom tracks to construct a detailed bathymetry map through interpolation in Surfer (Golden Software) (Figure 4A).

3.3 | Sediment sampling

Short cores with a length between 30 cm and 60 cm were collected using a UWITEC gravity coring device with hammer extension (Table 1) in January 2016. Nine cores (Gem01 (abc), Gem02–07) from seven sites were retrieved along a basin-longitudinal transect, starting from the outlet of the basin and moving northwards with incremental steps of 200–400 m (Figure 4). In order to compare the sedimentary content of the lacustrine cores with their subaerial counterparts and potential source areas, modern surface samples were gathered from the beach (Be), dunes (Du) and along the outlet (Ou) (Figure 2, Table 1).

3.4 | X-ray computed tomography

Closed cores were imaged with a Siemens SOMATOM Definition Flash medical X-ray computed tomography (CT) scanner at the Ghent University Hospital (UZ Gent). The CT scanner was operated at 120 kV with an effective 200 mAs and a 0.55 pitch. The scans were reconstructed into a DICOM image stack, representing a volume with voxel sizes of ~0.15 mm × ~0.15 mm × 0.60 mm. Each DICOM image stack was imported into the VG Studio v3.0 software package (Volume Graphics), which allows

20554877, 2025, 5, Downloaded from https://onlinelibrary.wiley.com/doi/10.1002/dep2.70031, Wiley Online Library on [16/12/2025]. See the Terms and Conditions (https://onlinelibrary.wiley.com/terms-and-conditions) on Wiley Online Library for rules of use; OA articles are governed by the applicable Creative Commons License

TABLE 1 Overview of sampling sites (hammer cores and surface samples).

Sample name	Short name	Latitude (S)	Longitude (W)	Sample type	Length (cm)	Water depth (m)	Extra info
Cores							
GEM16-01A-1H	Gem01(a)	40°04′17.52″	73°39′09.68″	Hammer core	31	5	–
GEM16-01B-1H	Gem01(b)	40°04′17.77″	73°39′09.57″	Hammer core	37	5	–
GEM16-01C-1H	Gem01(c)	40°04′17.80″	73°39′09.31″	Hammer core	47	5	–
GEM16-02A-1H	Gem02	40°04′15.66″	73°39′07.14″	Hammer core	30	10.5	Top missing
GEM16-03A-1H	Gem03	40°04′12.60″	73°39′06.00″	Hammer core	47	13	–
GEM16-04A-1H	Gem04	40°04′08.60″	73°39′04.18″	Hammer core	36	17.5	–
GEM16-05A-1H	Gem05	40°04′04.97″	73°39′03.72″	Hammer core	50	18	–
GEM16-06A-1H	Gem06	40°04′00.64″	73°39′05.55″	Hammer core	43	16.5	–
GEM16-07A-1H	Gem07	40°03′55.91″	73°39′07.27″	Hammer core	60	16	–
Surface samples							
GEM-Ou1	Ou1	40°04′19.75″	73°39′10.56″	Surface sample	–	–	Lake head
GEM-Ou2	Ou2	40°04′21.31″	73°39′11.53″	Surface sample	–	–	Wet outlet (creek)
GEM-Ou3	Ou3	40°04′22.30″	73°39′15.95″	Surface sample	–	–	Dry outlet, at position tree trunks
GEM-Ou4	Ou4	40°04′20.37″	73°39′17.76″	Surface sample	–	–	Sand layers
GEM-Du1	Du1	40°04′20.46″	73°39′10.71″	Surface sample	–	–	Dunes at lake head
GEM-Du2	Du2	40°04′22.91″	73°39′12.21″	Surface sample	–	–	Dunes at bend outlet channel
GEM-Be	Be	40°04′20.21″	73°39′24.65″	Surface sample	–	–	Beach

colour scale adjustments and the creation of digital volume cross-sections for analysis. Since the attenuation of the scanner's X-ray beam along its pathway depends on density as well as chemical composition (effective atomic number) of the sediment, CT scans help to distinguish individual stratigraphic units and to increase the visibility of three-dimensional structures, textures and components.

3.5 | Linescan photography and multi-sensor core logging

Cores were split, cleaned and photographed with a linescan camera attached to a Geotek Multi-Sensor Core Logger (MSCL) at the Renard Centre of Marine Geology (RCMG; Ghent University). Photographs in this publication have been contrast-enhanced (histogram equalisation in Corel Photo-Paint). Sediment surfaces were described macroscopically with attention to structures, textures and components that allow distinguishing background sedimentation from event deposits. Split cores were also logged with the MSCL to obtain values for magnetic susceptibility (MS) and gamma density, both with a downcore resolution of 2 mm. These sediment-physical properties help to identify and correlate deposits with contrasting geochemistry, grain-size and/or porosity, all of which relate to sediment provenance and transport processes.

3.6 | Grain-size analysis

Grain-size measurements were executed with a 1- to 2-cm resolution on master cores Gem01 (c) and 07, and on all surface samples from the beach, dunes and along the outlet channel. Sample pretreatment included a stepwise elimination of organic matter, calcium carbonate and biogenic silica by chemical treatment with H_2O_2, HCl and NaOH, respectively (see Text S1). These components were removed because the irregular and/or elongated shapes and density of such organic particles, shell fragments and diatom frustules lead to different aerodynamic and hydrodynamic properties compared to those of clastic grains, and would thus bias our interpretations on the transport and depositional processes. As the surrounding lithology does not contain carbonate-rich lithologies, we expect the HCl treatment to only remove biogenic fragments, such as shell debris. As a final step, Sodium Hexametaphosphate was added for a complete disaggregation of the sample. Grain-size distributions in volume% were obtained by a Malvern Mastersizer 3000 laser diffractometer at RCMG (Ghent University). Output data were transformed into

20554877, 2025, 5, Downloaded from https://onlinelibrary.wiley.com/doi/10.1002/dep2.70031, Wiley Online Library on [16/12/2025]. See the Terms and Conditions (https://onlinelibrary.wiley.com/terms-and-conditions) on Wiley Online Library for rules of use; OA articles are governed by the applicable Creative Commons License

grain-size statistical parameters with Gradistat 8.0 Excel software (Blott & Pye, 2001).

3.7 | XRF core scanning

XRF data were collected on master cores using the Avaatech XRF Core Scanner II at MARUM (University of Bremen), with a downcore slit size of 10 mm, using generator settings of 30 kV (for Br, Rb, Sr and Zr) and 10 kV (for Al, Si, S, K, Ca, Ti, Fe and Mn), a current of 0.75 and 0.20 mA and a sampling time of 20 and 15 s, respectively. Data were acquired by a Canberra X-PIPS Silicon Drift Detector (SDD; Model SXD 15C-150-500) with 150 eV X-ray resolution, the Canberra Digital Spectrum Analyzer DAS 1000 and an Oxford Instruments 50 W XTF5011 X-Ray tube with Rh target material. Raw data spectra were processed by the analysis of X-ray spectra by Iterative Least Square software (WIN AXIL) package from Canberra Eurisys. For further analysis, Ca, Sr, Br, S, Ti and Si were selected based on a visual assessment of the noise levels and presence of significant peaks in the raw count data over the whole scan. Selected element intensities were centred-log-ratio (clr) transformed to overcome the limitations of the double constrained data space, matrix effects and inhomogeneities throughout the cores (Weltje & Tjallingii, 2008). A principal component analysis (PCA) was performed to reduce the dimensions of the dataset. The loadings of the first two principal components (PCs), which explain most variance in the dataset, were visualised in a covariance biplot. This visualisation gives information about the relationships between selected elements and how much each element contributes to the PCs. On the scores of PC1 and PC2, Ward's hierarchical agglomerative clustering (Ward, 1963) was applied to independently classify parts of the core with geochemical similarity. For Gem01 and Gem07, we selected three and two clusters, respectively. The mean of each clr-transformed element over the whole core and within each cluster was calculated to further characterise each cluster additionally to the scores biplot. The deviation between both means represents the relative element content per cluster.

3.8 | Age control

Short-lived radionuclide data for ^{210}Pb and ^{137}Cs isotopes were obtained at the University of Bordeaux on sediment from Gem01 (c), and Gem07 to obtain age information for the sediments from the last ~100–150 years (Oldfield & Appleby, 1984). Measurements of ^{210}Pb, ^{137}Cs and ^{226}Ra activities were conducted on freeze-dried samples, utilising a low-background, high-efficiency, well-shaped gamma-ray detector (CANBERRA). Calibration of the gamma detector was achieved using certified reference materials (IAEA-RGU-1; SOIL-6). Due to extensive nuclear weapon testing between 1952 and 1963, radioactive fallout reached a maximum in 1965 in South America (Arnaud et al., 2006), causing a ^{137}Cs peak in lacustrine sediment records. In our cores, the measured $^{210}Pb_{ex}$ values were too low (between 0 mBq/g and 20 mBq/g) and did not show a monotonic exponential decay trend and thus were not used for calculation of sedimentation rates.

A total of eight macroscopic plant remains with C weights >1 mg were used for AMS-^{14}C dating at the ^{14}CHRONO Centre of the Queen's University Belfast (UK) (Table 2). Samples were subject to an acid–alkali–acid (AAA) 60°C pretreatment in order to strip carbonates (with HCl) and humic acids (with NaOH). Calibrated ages were calculated by applying the Southern Hemisphere atmospheric 'SHCal20' calibration curve (Hogg et al., 2020).

Age-depth models were constructed for deep basin core Gem07, using Bayesian statistics and auto-regressive Markov-chain Monte Carlo (MCMC) iteration algorithms embedded within BACON 2.2 software (Blaauw & Christen, 2011). Model input included the depths of the ^{137}Cs peak and uncalibrated radiocarbon ages (BP) with error ranges. A 'boundary' was set at 29.5 cm to allow a drastic change in sedimentation rate (discussion Section 5.1). Event deposits were removed before the modelling procedure using the 'slump' function in the BACON software. The used BACON priors (acc.shape: 2.2; acc.mean: 4.25; mem.strength: 10; mem.mean: 0.3; thick: 1) allowed a smooth accumulation model to be computed, which is visually consistent with peaks in the ^{14}C probability distributions.

4 | RESULTS

4.1 | Geomorphological processes at the outlet channel

Field observations and aerial imagery provide a general perspective on the processes that control the morphology and sediment sources at the outlet channel. The dunes covering the bedrock directly south of the outlet channel reach heights of 20–35 m a.s.l. Dune migration towards the lake outlet is evidenced by comparison of satellite images from 2011 and 2023 (Google Earth) with oblique aerial pictures from 1943 (Figure 3D). In 1943, the lake outlet was bordered by trees on bedrock, but these are now covered by North-propagating dunes. As a consequence, the southern lake shore at the outlet is now fully covered by dune sand. Dune migration is considered to be an ongoing process, as the 2023 picture

20554877, 2025, 5, Downloaded from https://onlinelibrary.wiley.com/doi/10.1002/dep2.70031, Wiley Online Library on [16/12/2025]. See the Terms and Conditions (https://onlinelibrary.wiley.com/terms-and-conditions) on Wiley Online Library for rules of use; OA articles are governed by the applicable Creative Commons License

TABLE 2 Overview of radiocarbon sampling locations and AMS ^{14}C dating results.

Sample name	Lab ID	Core	Depth (cm)	Pre-treatment[a]	Type	$F^{14}C$	Error (1σ)	^{14}C age (BP)	Error (1σ)	Cal.[b] age range (95.4%; BP)
G_a	UBA-34782	GEM16-06A-1H	35	AAA	Wood	0.9557	0.0035	364	29	468–310
G_b	UBA-35636	GEM16-07A-1H	30	AAA	Leaf and twig fragments	0.9924	0.0030	61	25	240–231 (2.3%) 139–113 (16.8%) 97–84 (2.2%) 71–24 (74.1%)
G_c	UBA-35637	GEM16-07A-1H	33	AAA	Leaf and twig fragments	0.9924	0.0030	158	25	269–217 (25.4%) 147–... (70.1%)
G_d	UBA-35638	GEM16-07A-1H	35	AAA	Leaf and twig fragments	0.9805	0.0030	104	25	252–227 (9.9%) 140–80 (30.7%) 75–... (54.9%)
G_e	UBA-35639	GEM16-07A-1H	41	AAA	Leaf and twig fragments	0.9872	0.0028	185	23	280–167 (51.3%) 155–134 (11.1%) 119–59 (21.6%) 28–... (11.4%)
G_f	UBA-35640	GEM16-07A-1H	44	AAA	Leaf and twig fragments	0.9772	0.0031	131	26	254–225 (15.3%) 141–... (80.1%)
G_g	UBA-35641	GEM16-07A-1H	50	AAA	Leaf and twig fragments	0.9645	0.0041	291	34	444–361 (29.2%) 332–276 (48.9%) 213–151 (17.4%)
G_h	UBA-34784	GEM16-07A-1H	58	AAA	Wood and twigs	0.9393	0.0039	503	33	545–486 (93.0%) 481–469 (2.5%)

[a]AAA, acid-alkali-acid (HCl-NaOH-HCl) method.

[b]Applied calibration curve is SHCal20.

20554877, 2025, 5, Downloaded from https://onlinelibrary.wiley.com/doi/10.1002/dep2.7003l, Wiley Online Library on [16/12/2025]. See the Terms and Conditions (https://onlinelibrary.wiley.com/terms-and-conditions) on Wiley Online Library for rules of use; OA articles are governed by the applicable Creative Commons License

shows a more extensive dune-covered shoreline (~115 m length covered by sand) compared to the 2011 picture (~80 m covered by sand).

Dunes also border the entire southern slope of the winding outlet channel. As observed at one location in January 2016 (summer season; Figure 2: picture 8), these dunes can cover the channel floor during dry (summer) periods, forcing the creek to locally continue subterraneously. In October 2024 (spring season), higher water discharge resulted in subaerial flow. Old tree trunks and debris (car tire, ropes) were observed halfway down the channel at ~1.1–1.5 m a.s.l., which is slightly above the level potentially reached by spring tides (Figure 2: picture 9; Figure 3E). These objects are interpreted as driftwood and debris transported into the channel by marine inundation, given that no large trees are present on the local forested slopes and no human settlements or roads are nearby (see Section 5.2). The position of the tree trunks changed a few metres between 2016 and 2024 (Figure 3E) and a significant portion of the sandy fill of the channel at this location was removed. About 40 m upstream of this location, a small 2 m high waterfall over sandstone (Cancagua) layers is present (Figure 2; picture 7), forming a knickpoint in the longitudinal stream profile (Figure 3C). The knickpoint has 2.2 m of relief and reaches ~4.4 m a.s.l., which is similar to the elevation of a coastal terrace probably associated with the mid-Holocene highstand in South-Central Chile, when relative sea level was about 4 m higher than at present (Garrett et al., 2020). The lake level was at a height of 5.88 ± 0.2 m a.s.l in October 2024. These geomorphic observations suggest that (i) coastal tectonic uplift processes are the main cause of the barrier and lake formation, (ii) subsequent fluvial incision shaped the outlet channel and (iii) dune dynamics may play a subordinate role.

4.2 | Hydro-acoustic mapping of the lake bottom

Outcropping bedrock formations along the basin slopes reflect most of the incoming SSS energy, leading to distinct zones with very high reflectivity (Figure 4). In addition, high intensity values are found in the shallow areas (~0–10 m depth) near the outlet channel and are interpreted as coarse-grained bottom sediments. Moreover, discrete high-backscatter patches with dimensions of ~5×5–20 m and with a prevailing NW-SE (i.e. downslope) orientation are spread across the southern area and are abruptly disappearing further to the north. Their strong reflectivity may be the result of a positive topography and/or a high reflectivity associated with a coarse lithology. Going further north from coring site Gem04, the lake bottom has a smooth low-reflectivity appearance on SSS imagery, which is typical for fine-grained sediments. A maximum water depth of ~18 m is observed around site Gem05.

4.3 | Lithology and correlation of sediment cores

Master core Gem07 (60 cm) was collected from the northernmost sampling site at a water depth of 16 m (Figure 4C, Table 1). It is composed of brown, silty gyttja, containing large quantities of macro-organic particles (Figures 5 and 6). Most of the organics can be identified as aquatic plant remains, but multiple pieces of wood, twigs and leafy material were observed as well. Sediment is largely composed of silt; 55–92 volume% (% vol), with a coarse silt mode and a variable sand admixture. Five depth intervals hold sand fractions that generally exceed 20 % vol, including coarse to very coarse sand; from top to bottom at a depth of: 0–6, 22–30, 34–35, 42–44 and 51–55 cm; and referred to as G1, G2, G3, G4 and G5, respectively. These sandy intervals have a yellow-beige to grey-beige sediment colour and are classified as s1 layers (blue sections in Figures 5 and 6). They coincide with (slightly) increased MS values, reaching 30×10^{-5} SI for layer G5, and attenuate more of the incoming X-rays, which translates to a brighter grey-scale on CT images. Overlying a characteristically sharp basal contact with or without erosional truncation, sand grains in G1–G5 show an overall fining-upward trend, eventually merging into a silty mud cap that blends into the overlying gyttja. Such gradual transition may complicate the identification of the layers' upper boundary, as is the case for G2. Deposits G1 and G5 display superimposed graded pulses (Figures 5 and 6). In addition to the sandy intervals G1–G5, the Gem07 record captures a few more intervals with a slightly increased sand content, that is, more than 15 % vol (Figure 6); at 7–9, 12–15, 45–46 and 47–48 cm (type s2). Compared to s1 layers, sand grains in these s2 layers are much more dispersed within the brown gyttja, resulting in a blurry appearance with poorly defined lower and upper boundaries and no clear expression on the CT images.

Basin wide correlations are based on macroscopic lithological characterisation and are supported by CT imagery and patterns in MS (Figure 5; Figure S2). Technical issues during the acquisition of core Gem02 caused the loss of its top section. When moving southward from coring site Gem07, towards the lake outflow, gyttja successions become overall thinner. In contrast, layers G1–G5 do not taper in shallower water, but

20554877, 2025, 5, Downloaded from https://onlinelibrary.wiley.com/doi/10.1002/dep2.70031, Wiley Online Library on [16/12/2025]. See the Terms and Conditions (https://onlinelibrary.wiley.com/terms-and-conditions) on Wiley Online Library for rules of use; OA articles are governed by the applicable Creative Commons License

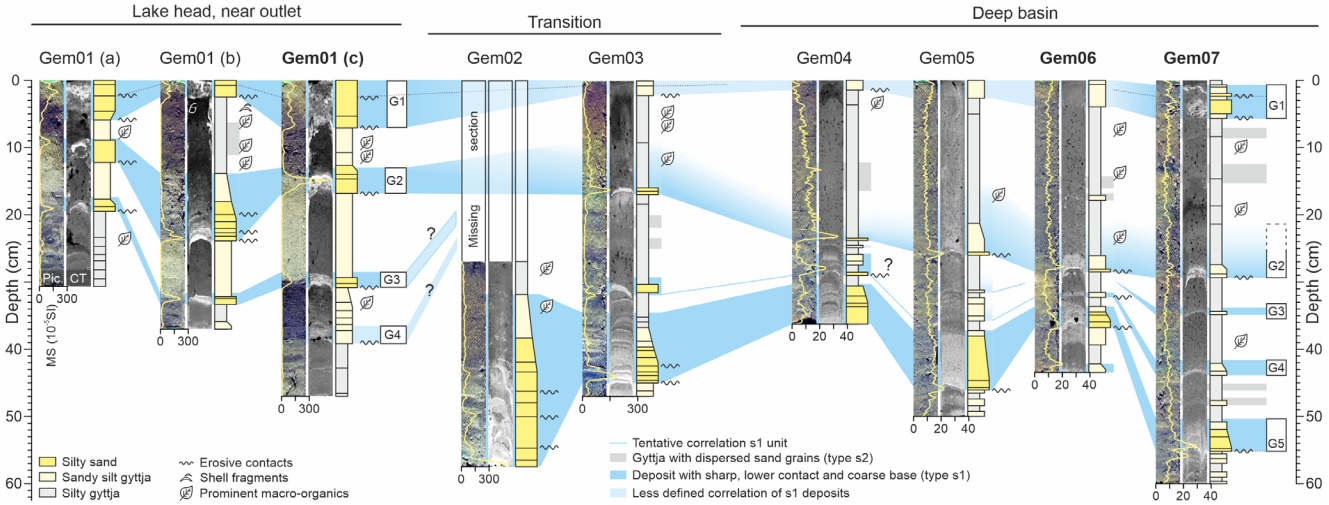

FIGURE 5 Core correlation in Laguna Gemela West. Depositional environments are separated in lake head (near outlet), transition zone and deep basin. For each core, photograph (contrast enhanced), CT image, lithology and magnetic susceptibility (MS) are presented. Note the different MS scaling for the deep basin cores. Correlations are mainly supported by the lateral continuity of prominent sand layers of type s1 (blue), accompanied by increased MS values and stronger X-ray attenuation when compared to the organic gyttja in which they are embedded. Correlation of the lake outlet cores is further supported by the colour and type of the sedimentation between s1 layers. Question marks and light blue colour represent correlation uncertainties. Support by CT-density values for the correlation of G3, G4 and G5 between core Gem01(c) and Gem07 can be found in Figure S2.

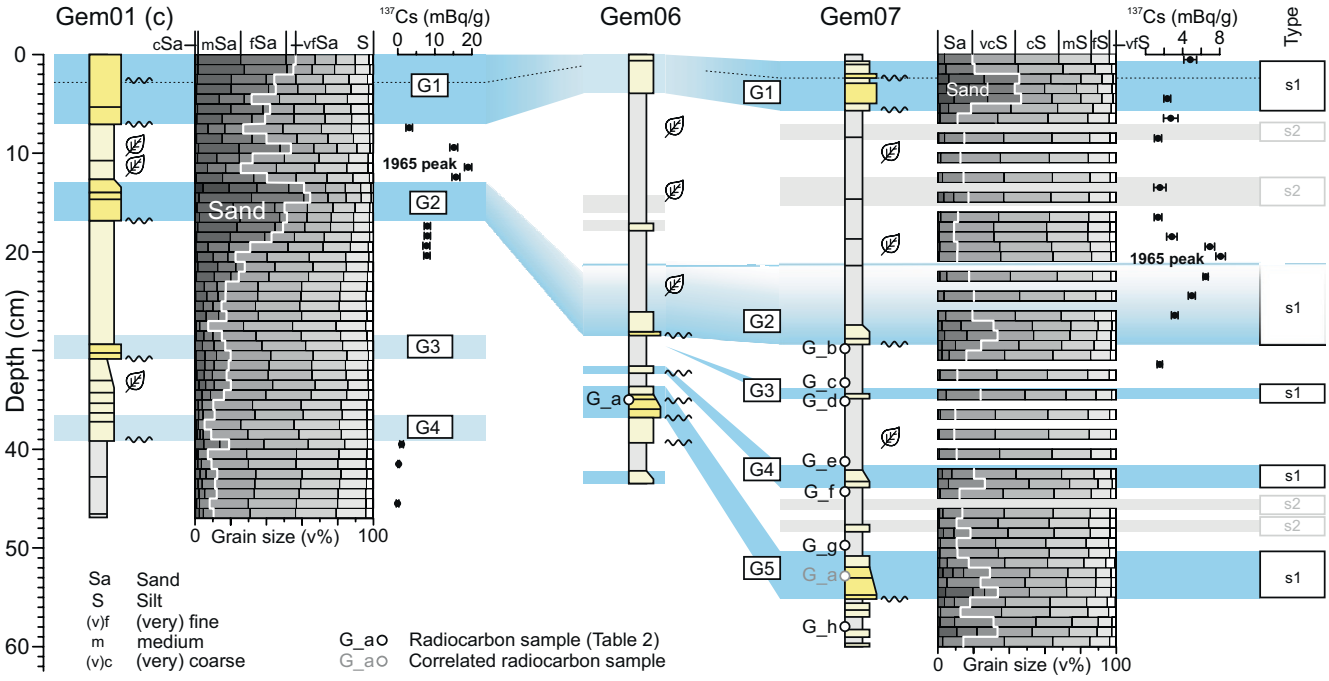

FIGURE 6 Grain-size data and ^{137}Cs data of two master cores. Profiles of ^{137}Cs in Gem01 (c) and Gem07 both show peaks just above layer G2, interpreted to be the maximum bomb testing fallout in 1965 CE, supporting the core correlation for the G2 layer. A total of eight radiocarbon samples were collected from Gem06 and Gem07, and used for establishing an age-depth model for core Gem07. Grain-size data show an overall higher sand content in Gem01 and higher sand content in each s1-type layer. It has to be noted that the organic content was removed prior to grain-size analysis.

maintain a constant thickness or become even thicker and/or more prominent, displaying an increasing sand fraction and an increasing density contrast to the under- and overlying gyttja. Each of these sandy units possesses a certain degree of internal layering and lamination, which is particularly notable for G5 in cores

20554877, 2025, 5, Downloaded from https://onlinelibrary.wiley.com/doi/10.1002/dep2.70031, Wiley Online Library on [16/12/2025]. See the Terms and Conditions (https://onlinelibrary.wiley.com/terms-and-conditions) on Wiley Online Library for rules of use; OA articles are governed by the applicable Creative Commons License

Gem02 and -03, where CT imagery reveals multiple stacked sheets of sand and silt. In ocean-proximal sites (Gem01, -02 and -03), MS peaks reach much higher values than in the deep basin where a non-magnetic, organic admixture prevails; 450×10^{-5} SI versus 30×10^{-5} SI. In the deep basin, the stratigraphic column remains similar from site Gem07 up to Gem04. Thick sand layers G1, G2 and G5 can be correlated confidently, whereas thinner layers G3 and G4 are much more difficult to identify laterally. Dispersed sand intervals of type s2 are not of consistent occurrence throughout the lake basin, in terms of prominence, thickness and location.

Deposits in Gem01 (abc) differ from the other coring sites by displaying additional facies changes, which are not observed in the deeper basin. Highly organic gyttja composes the interval between G1 and G2, whereas a light beige, homogeneous deposit with low MS values occurs between G2 and a lower lying type s1 sand layer (Figures 5 and 6). This beige, sandy silt facies is low in organics and is consistently present in all three cores from site Gem01. Below G3 in Gem01, another interval of brown gyttja covers about 5 cm, below which a normally graded, 4-cm thick silty deposit can be found (G4). This dark grey layer has an increased CT density and sharply interrupts the underlying, layered gyttja. Based on a similarity in CT density (average value = 174 HU in Gem01 and 178 HU in Gem07, see Figure S2) and low number of gas cracks, the equivalent of this underlying gyttja can be identified between G4 and G5 in core Gem07. This correlation is further supported by a consistent decrease in CT values from G4 to G3 in both cores. Overall, the rather similar CT density trends in the sediments between G3, G4 and G5 in cores Gem01 (c) and Gem07 strengthen our proposed correlation.

4.4 | XRF core scanning data

Due to high water content and sediment cracks, the XRF scanning data are relatively noisy and element plots do not show simple patterns for interpretation (Figure S3). However, the results of the PCA and cluster analysis enable distinction of different geochemical stratigraphic units that correspond to the lithological observations (Section 4.3) and contribute to the interpretation of the units in terms of sedimentological processes (Section 5.2). All the s1 layers in both shallow and deep basin cores are classified in a single cluster (coloured 'yellow' in Figure 7), which contains relatively high values of Ca and Sr. The signature of s2 layers is unclear as some are classified in the 'yellow' cluster, whereas other s2 layers correspond to the 'green' cluster. The latter is characterised by relatively high Si and Ti contents. The macroscopically observed changes in sediment type in between the s1 layers in the shallow core Gem01 are also reflected in an alternation of cluster attributions. Whereas the interval G2–G3 and below G4 correspond to the 'green' cluster (high in Si and Ti), the highly organic intervals G1–G2 and G3–G4 form a 'red' cluster that is dominated by high values of Br. From an inorganic geochemistry perspective, the unit between G2 and G3 in Gem01 (c) is thus comparable to the units between S1 layers in the deep basin core Gem07 and the 'red' cluster dominated by Br seems to be an exclusive feature of the shallow southern area.

4.5 | Surface samples and grain-size comparison to sediment cores

Surface samples collected along the narrow, winding channel between the Pacific Ocean and Laguna Gemela West (Figure 2) possess nearly identical grain-size distributions, holding a main population of well-sorted sand between 100 µm and 900 µm with a mode of 340–400 µm (Pop. 3: sand) and a minor, secondary population between 1 µm and 20 µm with a mode of 5–7 µm (Pop. 1: clay-fine silt) (Figure 8). MS point measurements on subaerial sands vary between 470 and 790×10^{-5} SI, with an average of ~590×10^{-5} SI. The Gemelas beach sands in front of the outlet channel (sample Be in Figure 2) comprise olivine, pyroxene, magnetite, hornblende and other less important trace (heavy) minerals, most of which hold a significant amount of iron in their crystal structure. Weathering of these iron-rich sands or sandstones provides a reddish rust coloured hue, as observed along parts of the Gemelas outlet channel, for example, in samples Ou2 and Ou4 (Figure 2). Calcareous shell hash constitutes the most prominent allochemical component.

The lacustrine gyttja samples from Gem07 mainly plot in between grain-size populations Pop. 1 and Pop. 3, containing silt and very fine sand between 4 µm and 100 µm with a mode of 22 µm (Pop. 2) (Figure 8). Type s1 deposits from ocean-proximal core Gem01 (c) and ocean-distal core Gem07 have bimodal distributions with a coarse mode at 300–400 µm or 100–300 µm, respectively, and a fine mode at 20–30 µm. This potentially reflects the commixture of both terrestrial surface sediment and gyttja. Elevated MS values in s1 layers confirm the influence of magnetic minerals as present within the surface sands. The s2 layers include a small sandy distribution tail (at 230 µm), that is, given the dispersed nature of the sand grains, much less significant than in s1 units where it forms a clear distribution peak (mode).

20554877, 2025, 5, Downloaded from https://onlinelibrary.wiley.com/doi/10.1002/dep2.70031, Wiley Online Library on [16/12/2025]. See the Terms and Conditions (https://onlinelibrary.wiley.com/terms-and-conditions) on Wiley Online Library for rules of use; OA articles are governed by the applicable Creative Commons License

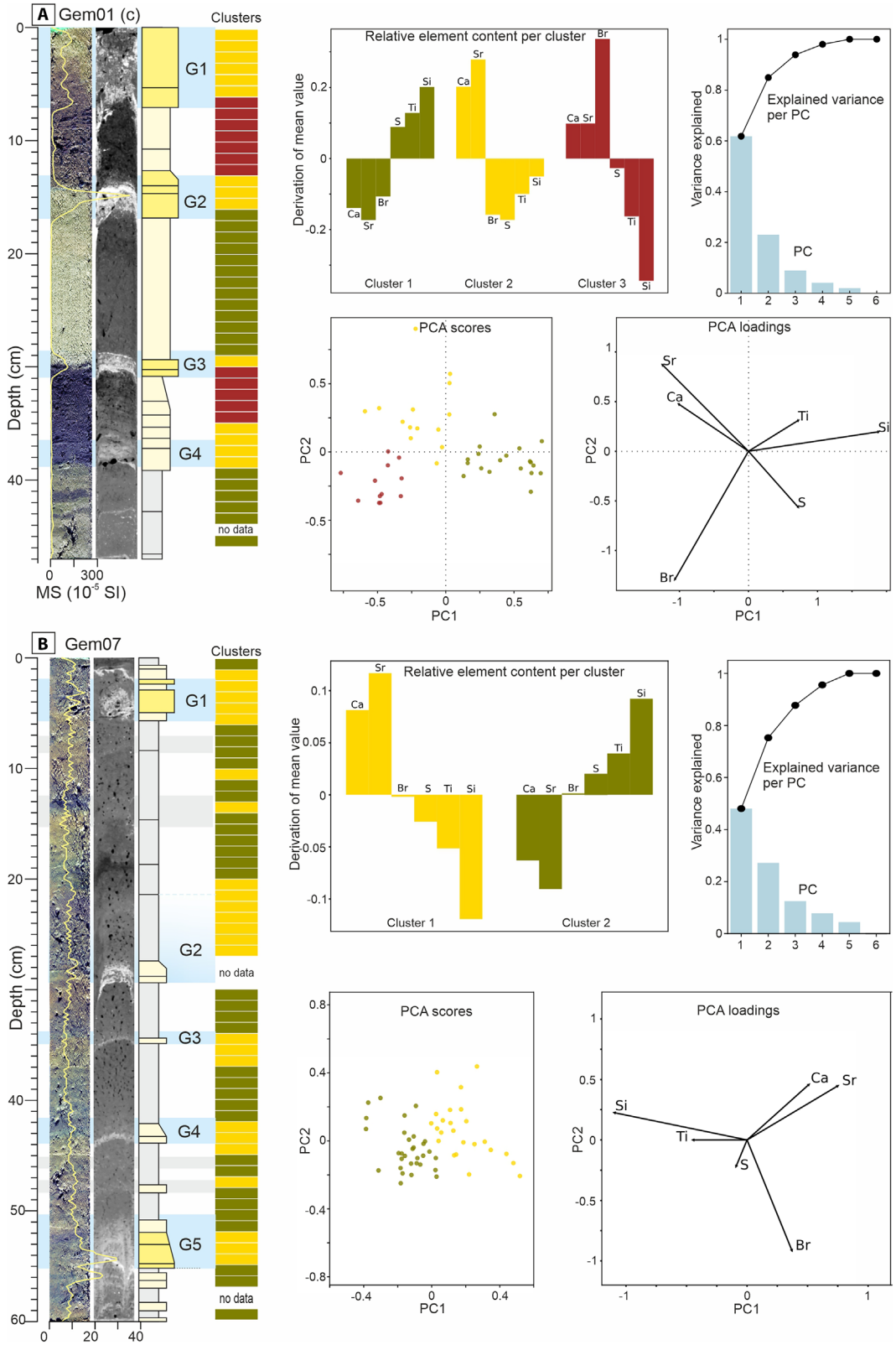

FIGURE 7 Multivariate statistical analysis of XRF data obtained on (A) core Gem01 (c) and (B) core Gem07. Left side: For each core, the enhanced core picture, magnetic susceptibility, CT-scan image and schematic lithology are presented next to the colour-coded clusters derived from the XRF data (1 cm measurement resolution). Right side: Explained variance for each PC of the PCA analysis, together with the PCA scores of each XRF data point and the PCA loading of each element in the PC1-PC2 space. Cluster analysis of the PCA data shows three or two main clusters for Gem01 (c) and Gem07, respectively. The relative element content of each cluster is represented as the deviation of the mean clr values of each element per cluster from the mean clr value of that element over the entire core.

20554877, 2025, 5, Downloaded from https://onlinelibrary.wiley.com/doi/10.1002/dep2.70031, Wiley Online Library on [16/12/2025]. See the Terms and Conditions (https://onlinelibrary.wiley.com/terms-and-conditions) on Wiley Online Library for rules of use; OA articles are governed by the applicable Creative Commons License

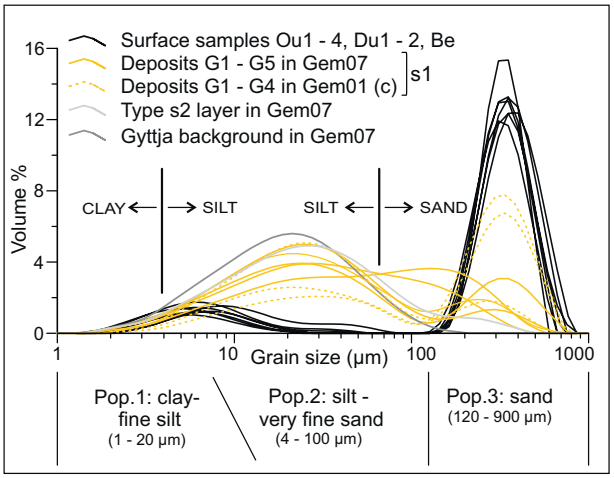

FIGURE 8 Grain-size distributions of surface samples compared to lacustrine deposits. For illustrative clarity, we selected one representative sample for the S2 deposits and for the Gyttja background. Distributions are divided into three populations; Pop. 1: Clay to fine silt (1–20 µm), Pop. 2: Silt to very fine sand (4–100 µm) and Pop. 3: sand (120–900 µm). Pop. 3 dominates the surface samples and s1-type layers in the lake head core Gem01(c). The s1 layers (G1–G5) in the deep basin core Gem07 have a broad grain-size distribution containing a significant portion of all three populations.

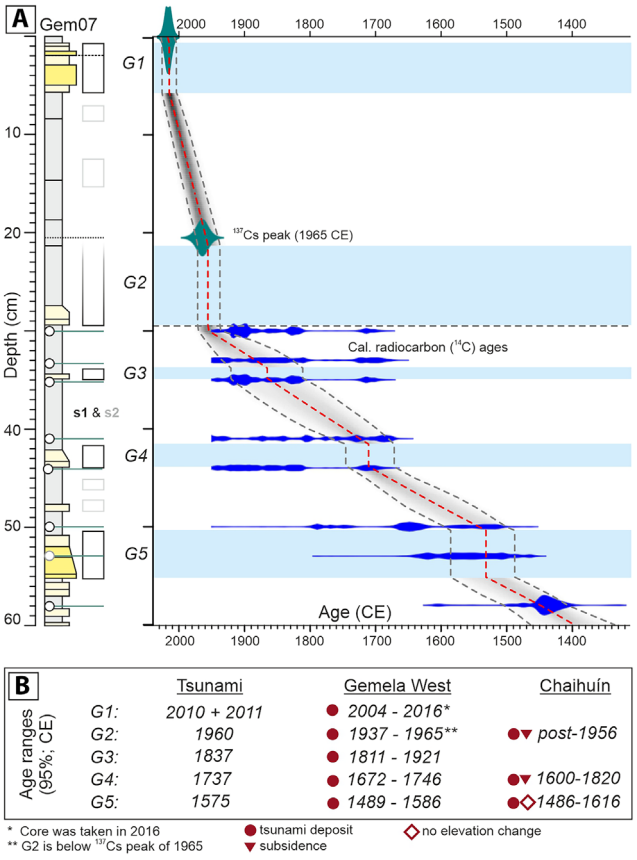

FIGURE 9 (A) Age-depth model of deep basin core Gem07 based on radionuclide data (^{137}Cs and ^{14}C). The model was calculated in Bacon Software and s1 layers were regarded as instantaneous deposits. The probability distribution of the calibrated ^{14}C ages is coloured in blue. The green-coloured normal distributions represent the core top and the ^{137}Cs peak corresponding to the maximum fallout in CE 1965. (B) 95% confidence age range of the s1 deposits extracted from the age-depth model and compared to the age ranges of published event horizons (tsunami deposits, coseismic elevation changes) from the nearby Chaihuín site (Hocking et al., 2021) and attribution to historically documented tsunami events.

4.6 | Age-depth model of the master core

Deposits in core Gem07 from Gemela West display a well-developed ^{137}Cs peak of 8 mBq/g at a depth of 20.5 cm (Figure 6), representing the CE 1965 peak fallout of nuclear bomb testing. Values of ^{137}Cs increase again slightly in the topmost 6 cm of the core, which may be due to sediment reworking of older deposits during the formation of layer G1. In core Gem01 (c), ^{137}Cs culminated at 1.5 cm above unit G2, thereby independently confirming the correlation of G2 between the different depositional settings.

Eight radiocarbon ages serve to extend the age-depth model for core Gem07 beyond CE 1965 (Figure 9A, Table 2). Due to a calibration plateau for atmospheric ^{14}C throughout the last ~300–400 years, most calibrated age ranges are wide and the probability distributions include multiple peaks. The two oldest ages are older than the ^{14}C calibration plateau and are crucial to constrain sedimentation rates in the core. The model for Gem07 suggests much higher sedimentation rates for the uppermost 20 cm of the core (~2.8 mm/year), compared to its lower part (~0.4 mm/year). Sedimentation rates have not been corrected for pore water content. Based on the model, the 95% confidence ranges of sandy s1 units were extracted and result in the following ages: G1: 2004–2016, G2: 1937–1965, G3: 1811–1921, G4: 1672–1746 and G5: 1489–1586 (Figure 9B). It has to be noted that, for G1 and G2, we narrowed down the younger limit of the age range because (i) the core was taken in CE 2016, and thus, G1 cannot be younger than this age, and (ii) G2 lies below the ^{137}Cs peak and thus must be older than CE 1965.

5 | INTERPRETATION AND DISCUSSION

5.1 | Evolution of the lacustrine sedimentary environment

We interpret the organic-rich silty sediments (gyttja) as continuously accumulated background sedimentation. The high organic content can be explained by the lack of

20554877, 2025, 5, Downloaded from https://onlinelibrary.wiley.com/doi/10.1002/dep2.70031, Wiley Online Library on [16/12/2025]. See the Terms and Conditions (https://onlinelibrary.wiley.com/terms-and-conditions) on Wiley Online Library for rules of use; OA articles are governed by the applicable Creative Commons License

main inflows and available clastic sediment sources in the densely forested fluvial catchment. Organic matter deposition mainly originates from (i) soil erosion and terrestrial plant debris, and its subsequent surface-runoff to the lake by high precipitation events, (ii) aquatic plant debris, (iii) biogenic productivity (diatoms) and (iv) other microorganisms. Sediment focusing processes explain why the gyttja units are thicker in the deeper sites of the lake and gradually taper out towards the shallower southern sites. Therefore, the highest resolution sedimentary record was obtained in site Gem07, for which we constructed the master age-depth model. The use of an auto-regressive approach for the age-depth modelling, representing the continuous sedimentation process, served well in circumventing the problem of multiple peaks in the probability distributions of the calibrated ^{14}C dates (Figure 9). Higher sedimentation rates for the uppermost 20 cm could relate to the typically water-rich less consolidated nature of the topmost organic sediments compared to deeper sequences, although this process does not explain the sevenfold increase in sedimentation rates. Overall, precipitation in the region decreased in the last decades, which would rather have led to a reduction in soil erosion and sedimentation rates. For example, in Valdivia, the trend in annual precipitation declined from 1850 to 1590 mm/year from 1979 to 2024 (Meteoblue, 2025). A comparable fivefold increase in sedimentation rates and increase in organic content was found in coastal Chilean lake Lanalhue (37.9°S), where detailed core studies and catchment analyses attested that intense forestry activities led to significant soil erosion and transport towards the lake since CE 1950 (Alaniz et al., 2021). For Gemela West, even though we lack chronological control within the past 50 years, detailed information on land use in the catchment and specific sedimentological analysis, we suggest a similar process in which intense forestry activities (in the 1990s) in the outer regions of the lake catchment may have led to substantial plant debris and soil erosion, explaining the significant increase in sedimentation rates of organic-rich background sediments.

The cores near the lake outlet (Gem01 site, 5 m water depth) show variable lithofacies and chemical composition throughout background sediments. In combination with the overall high reflectivity of the side scan sonar data and numerous high-reflectivity patches, the southern shallow lake area can be expected to represent a dynamic near-shore depositional environment. Mapping of macrobenthos in Laguna Gemela West in 2008 revealed a dense coverage of charophyte algae on the lake bottom near the outlet between 2.5 m and 7.5 m water depth (Palacios, 2008). As these observations were made before the deposition of the G1 sandy deposit (see Section 5.3), we can directly associate the highly organic facies at Gem01 (7–13 cm core depth) to the decomposition of benthic algae mats. These depositional units form their own geochemical cluster ('red') with elevated Br content. Possibly, the high organic content of the units enabled the sorption and binding of bromine that could have been brought in via sea water (e.g. Joe-Wong et al., 2019). The lithological changes from G3 upwards in these Gem01 shallow water sites could relate to local variability in charophyte algae abundance due to changes in lake level and water transparency or could relate to dune dynamics, such as dune propagation towards the site and subsequent erosion. Deeper sites are much less affected by these processes, and thus, properties of background sedimentation in Gem07 are stable over time.

In all cores, background sedimentation is repeatedly interrupted by s1 deposits, which we interpreted as 'instantaneous' event deposits and thus did not take part in the age-depth modelling procedure (Section 3.8). This interpretation is based on their elevated sand content, fining-upwards grading and especially a sharp base with signs of erosional scouring. These characteristics point towards deposition by a high-energy flow that is capable of transporting sand grains and eroding underlying sediments, followed by a waning of the flow speed allowing finer grains to settle (e.g. Sabatier et al., 2022). In contrast, s2 deposits are not considered event deposits as the sand grains are dispersed in an organic-rich matrix and layer boundaries are gradual and/or unclear. Their grain-size distribution shows the relatively small contribution of the sand grains compared to a dominant gyttja matrix (Figure 8). A probable origin for s2 layers in Gemela West may be episodes of enhanced wind-blown transport of dune sand into the lake. Accordingly, the s2 layers were not removed for age-depth modelling.

5.2 | Origin of event deposits

Lacustrine event deposits can be formed by a multitude of processes (Sabatier et al., 2022). In a coastal lake setting, the main mechanisms are storms, tsunamis, mass movements, run-off and river floods. Several lines of evidence attest that the s1 layers contain a large portion of beach and dune material that was transported into the lake via the outlet channel and are thus not related to mass movements or river floods, but to marine inundation events:

I Grain-size (Figure 8): Population 3 (sand content) in s1 deposits near the outlet shows the same mode and well-sorted distribution shape as the surface samples from the outlet channel, dunes and beach. Deep basin s1 sands have a much broader distribution, indicating

20554877, 2025, 5, Downloaded from https://onlinelibrary.wiley.com/doi/10.1002/dep2.70031, Wiley Online Library on [16/12/2025]. See the Terms and Conditions (https://onlinelibrary.wiley.com/terms-and-conditions) on Wiley Online Library for rules of use; OA articles are governed by the applicable Creative Commons License

mixture with gyttja lake sediments represented by population 2.

II Mineralogy: s1 deposits in the core sites near the outlet show the highest MS values of ~150 (10^{-5} SI) with a peak of about 500, which is only slightly below the average MS value of 590 for all surface samples (outlet/beach/dune). s1 deposits in the deep basin have much lower MS values of 20–30, indicating mixture with low MS gyttja lake sediments.

III Inorganic geochemistry: s1 deposits all fall into the 'yellow' cluster which contains relatively high values of Ca and Sr. As the lake catchment consists of sedimentary rocks poor in these elements, we interpret the s1 XRF scanning data as a signature for shell hash material, observed in the beach samples, which is transported into the lake (see e.g. Chagué-Goff et al., 2017). Turbidites related to mass movements or run-off would not be enriched in these elements and typically show a simpler grain-size evolution, reflected in homogenous or monotonously changing element data obtained by XRF scanning (Koutsodendris et al., 2023; Sabatier et al., 2022). The XRF scanning data of s1 deposits in Gemela West show a much more heterogenous nature (see Figure S3).

The strongest argument is related to the spatial distribution of these characteristics: The s1 deposits are coarser, thicker and have higher MS near the outlet channel when compared to the deeper basin sites. Close to the outlet, the event deposit thus mainly contains transported beach, dune and channel material, whereas in the deeper basin, the transported terrestrial sediments are mixed with organic-rich lake sediments. This all points to sudden sediment transport via the outlet channel into the lake by a marine inundation. Marine inundation of the lake via overwash of the bedrock (north of the channel) or dune-covered bedrock (south of the channel) can be excluded due to the elevation of these features, that is, 40–55 m a.s.l. and 20–35 m a.s.l., respectively (Figure 3B). As we do not have data from microfossil analysis (e.g. marine diatoms or foraminifera), it is currently not possible to evaluate whether offshore sediment sources (e.g. shoreface) potentially contributed to the event deposits, which would further support our interpretation (Sabatier et al., 2022).

The G2 deposit in Gemela West is located directly below the ^{137}Cs peak related to CE 1965 measured in both cores Gem01(c) and Gem 07. We interpret the CE 1960 tsunami as the cause for the G2 marine inundation deposit, because this tsunami had a reported run-up height of 10 m in the region (Figure 1), which is much more than required to have inundated the lake, and tsunami deposits have been found in several coastal sites between 38.3°S and 42.6°S in Chile (León et al., 2023). For example, sediment cores from the coastal lakes Cucao and Huelde (Figure 1; Kempf et al., 2015) show very similar sedimentological data, spatial patterns, and also relationships to terrestrial surface samples for the inferred CE 1960 tsunami deposit as obtained for Laguna Gemela West.

Distinguishing between extreme storm deposits and tsunami deposits can be challenging in some settings (Morton et al., 2007). However, the following arguments support tsunamis from megathrust earthquakes over inundation by storms as the source of the s1 deposits. First, we can confidently rule out hurricane-type storm surges, as tropical cyclones do not occur along the Chilean coast (Pillay & Fitchett, 2021). Second, wind waves are also unlikely sources. Even if extreme in height, their wave periods are probably too short (<30 s) to effectively inundate through the 400 m winding channel and reach the lake at an elevation of 5–6 m a.s.l. This implausibility remains even if very large wind waves coincide with other sea-level oscillations often associated with local coastal storms, as for example, occurred during the 2015 coastal storm in central Chile, one of the most intense in the country's recorded history (Winckler et al., 2017). This storm involved a combination of very large wind waves, storm surges and meteotsunamis, of which the latter two were triggered by different atmospheric pressure and wind patterns (Carvajal, Cisternas, et al., 2017; Carvajal, Contreras-López, et al., 2017). In order to provide a reference for the sea-surface elevations induced by this type of event, the top panel of Figure 10D shows the recorded sea level at Bucalemu, where the highest levels were observed (Carvajal, Cisternas, et al., 2017; Carvajal, Contreras-López, et al., 2017). The sea level reached approximately ~1.2 m above mean sea level due to the combined effects of a −0.15 m tide (red line), meteotsunamis up to 0.8 m (green line) and a storm surge of ~0.6 m (black dashed line).

Laguna Gemela West is located 630 km south of Bucalemu, where coastal storms are expected to have differing impacts. To evaluate the potential for storm-related inundation, we analysed sea-level records from the two nearest tide gauge stations, Corral and Bahía Mansa, using data from the IOC Sea Level Monitoring Facility (Flanders Marine Institute (VLIZ), 2024). These records, while covering a much shorter timeframe than the sedimentological record (2008–present in Corral; 2011–present in Bahía Mansa), show no sea-level oscillations comparable to the 2015 Bucalemu event, except during three tsunami events: the 2010 Chile regional tsunami (1.6 m a.s.l. in Corral; Figure 10A), the 2011 Japan far-field tsunami (1.6 m a.s.l.; Figure 10B) and the 2022 Tonga volcanic tsunami (1.2 m a.s.l.; Figure 10C). When comparing the amplitudes

20554877, 2025, 5, Downloaded from https://onlinelibrary.wiley.com/doi/10.1002/dep2.70031, Wiley Online Library on [16/12/2025]. See the Terms and Conditions (https://onlinelibrary.wiley.com/terms-and-conditions) on Wiley Online Library for rules of use; OA articles are governed by the applicable Creative Commons License

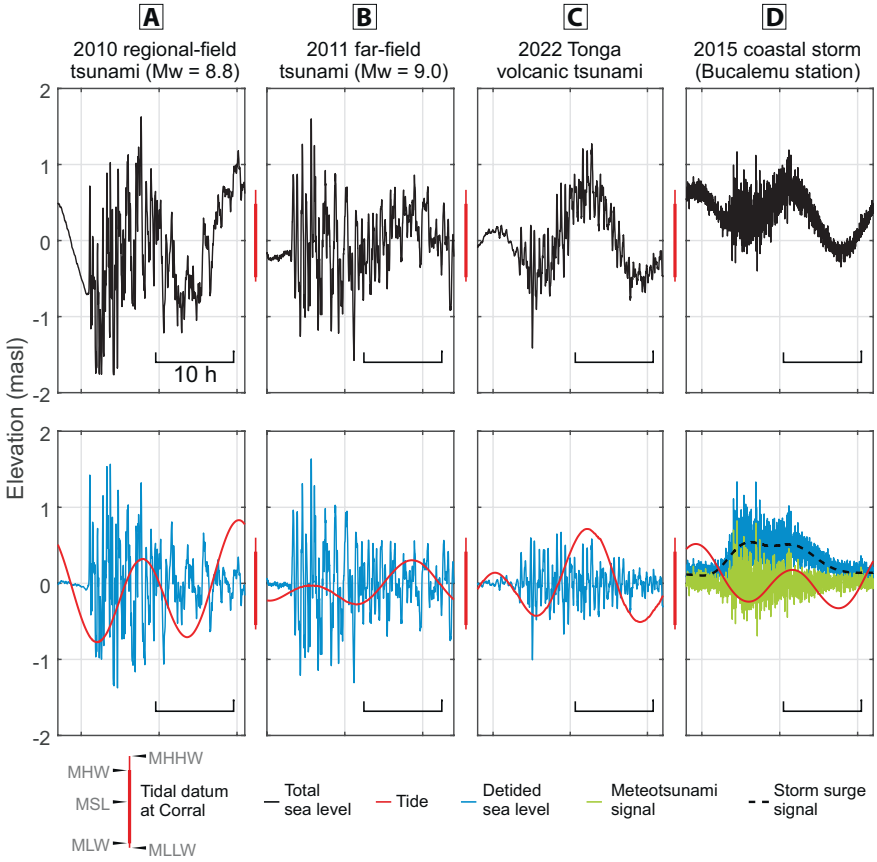

FIGURE 10 (A) Upper panel: Sea level recorded at Corral tide gauge after the CE 2010 earthquake, showing the tsunami signal. The red lines indicate relevant tide datums (see legend). MHHW, mean higher high water. MLLW: mean lower low water. MHW: mean high water. MLW: mean low water. MSL: mean sea level. Lower panel: Detided sea level (blue) and tide (red). (B) Same as A but for the CE 2011 far-field tsunami. (C) Same as A but for the CE 2022 Tonga tsunami. (D) Same as A but for the CE 2015 coastal storm recorded at Bucalemu tide gauge, where recorded sea levels were largest. The total sea level (black) resulted from the superposition of tide (red), storm surge (black dashed line), meteotsunamis (green) and large short-period wind waves (not recorded by tide gauge). Modified after Carvajal, Cisternas, et al. (2017) and Carvajal, Contreras-López, et al. (2017).

recorded at Bucalemu during the 2015 extreme coastal storm with those three tsunami events recorded at Corral, it is evident that, even under extreme conditions, storm-related inundations are less likely than tectonic tsunamis to reach the lake at an elevation of 5–6 m a.s.l. Also, the exceptional 2022 Tonga volcanic tsunami, the first volcanic event which generated worldwide tsunami signatures since the 1883 Krakatau event in the Sunda Strait (Hu et al., 2023), did not reach the same height in Corral station as the 2010 and 2011 tectonic tsunamis. After detiding the data, its tsunami signal has a maximum amplitude of only 0.7 m compared to 1.6 m for the 2010 and 2011 tectonic tsunamis. In addition to this lower amplitude at Corral, the 2022 Tonga tsunami waves were characterised by generally shorter wave periods (Lynett et al., 2022), making them less probably to inundate the elevated lake. Consequently, tsunamis generated by near, regional or remote megathrust earthquakes remain the most plausible mechanism for marine inundation of Laguna Gemela West. In turn, the impact of storm-related inundation or the 2022 Tonga volcanic tsunami may be constrained to the lower stretch of the outlet channel (0.5–2.5 m a.s.l.; below the barrier), potentially explaining the slight upstream position change of heavy tree trunks and debris in this part of the channel between the observations in 2016 and 2024 (Figure 3E). Inundation by spring tides alone does not reach these locations.

5.3 | Correlation to historical tsunamis

We tested if event layers of s1 type correlate to historically reported earthquakes and/or tsunamis since the middle of the 16th century in South-Central Chile (Cisternas et al., 2017). Compared to the more ocean-proximal locations, the deeper basin sites remained better protected from shallow water processes, macrobenthos activity and associated facies shifts (Section 5.1) and/or potential erosion by incoming extreme wave events (Section 5.2). Therefore, our master core is the one located at the most ocean-distal position in the deep basin (Gem07).

20554877, 2025, 5, Downloaded from https://onlinelibrary.wiley.com/doi/10.1002/dep2.70031, Wiley Online Library on [16/12/2025]. See the Terms and Conditions (https://onlinelibrary.wiley.com/terms-and-conditions) on Wiley Online Library for rules of use; OA articles are governed by the applicable Creative Commons License

All age ranges for the s1 deposits can be linked to known historical megathrust earthquakes and associated tsunamis that affected the region, and no historical tsunamis in the region are missing from the record (see also Section 5.4.3):

G5 (CE 1489–1586) can be linked to the giant CE 1575 earthquake. This is considered the predecessor of the CE 1960 earthquake, as historical and sedimentary evidence suggests a rupture length of *ca* 1000 km (Figure 1; Wils et al., 2020) and tsunami deposits were found in all suitable coastal archives, including the nearby Chaihuín site (Hocking et al., 2021). In Gem07, G5 is the most prominent event deposit in terms of thickness, CT density and MS. Multiple sand pulses at sites Gem02–03 (transition area) and Gem06–07 (deep basin) occur in the G5 deposit and may be caused by successive wave inundations during this tsunami event. A similar interpretation was proposed for multiple sand pulses in, for example, the CE 1960 tsunami deposit in Lake Huelde in South-Central Chile (Kempf et al., 2015) and for the 8.2 ka BP Storegga tsunami deposits in coastal lakes in western Norway (Bondevik et al., 1997).

G4 (CE 1672–1746) is less prominent than G5 and can be linked to the CE 1737 earthquake, of which seismic shaking is known to have severely damaged the town of Valdivia (Lomnitz, 1970). Even though written reports of a tsunami have not been found (Cisternas et al., 2017), the identification of ~0.2 m of subsidence in combination with a tsunami deposit dated to CE 1600–1820 at the Chaihuín site led to the interpretation of the 1737 megathrust earthquake indeed being tsunamigenic (Hocking et al., 2021). The more precise age range of G4 in Gemela West (CE 1672–1746; 95% confidence interval) provides additional support for a tsunami in CE 1737. An alternative hypothesis would be to link the tsunami deposit in Gemela West and Chaihuín to the more northern CE 1751 earthquake and tsunami (Figure 1). This event is regarded as the predecessor of the CE 2010 M_w 8.8 Maule earthquake (Udías et al., 2012). It produced a large tsunami that is well described in historical records with sedimentary evidence found as far south as Tirúa (38.3°S; Dura et al., 2017). However, the date of this event falls closely outside the age range of G4. Moreover, this alternative explanation is inconsistent with marsh subsidence (~0.2 m) in Chaihuín, inferred from comparing diatom assemblages directly below and above the tsunami deposit (event B) and the application of an updated regional transfer function which quantitatively relates diatom assemblages along the South-Central Chilean coast to marsh surface elevation (Hocking et al., 2021). This evidence of coseismic subsidence indicates that the tsunami was associated with megathrust rupture at the latitude of Chaihuín. Even when uncertainties in the diatom-derived relative sea-level changes would have led to an incorrect association of event B in Chaihuín to the CE 1737 event, a link to the CE 1751 event would generate additional inconsistencies. For example, it would be difficult to explain the absence of tsunami deposition in CE 2010 in Chaihuín while having tsunami deposits in Chaihuín and Gemela West for the CE 1751 event. So far, there is no robust evidence that a CE 1751 tsunami wave would have been significantly higher than in CE 2010 in our study area. From a seismic ground shaking perspective, inland lakes at the same latitude of our study area show modestly sized seismo-turbidites for the CE 2010 event, but no seismo-turbidites for the CE 1751 event (Moernaut et al., 2014), suggesting that the CE 1751 event ruptured less far south than the CE 2010 event. Even though none of the abovementioned arguments is conclusive on its own, together—and especially the sedimentary record of the nearby Chaihuín site—they offer a reasonable base to reject an association of the G4 deposit with the CE 1751 event and provide better support for the CE 1737 event to have formed G4.

G3 (CE 1811–1921) is also less prominent than G5 and can be linked to the CE 1837 megathrust earthquake. Historical and sedimentary evidence show coastal elevation changes and a tsunami between 41.9°S and 46.6°S (Cisternas et al., 2017). Together with the large far-field tsunami heights reported at different places around the Pacific, this attests to a high magnitude for this earthquake (~M_w 9.2; Abe, 1979; Carvajal, Cisternas, et al., 2017) that probably ruptured the southern half (41.2–46.6°S) of the CE 1960 rupture area (Figure 1; Cisternas et al., 2017). The high magnitude of this earthquake is further indicated by severe shaking in Valdivia (39.8°S) and the presence of seismo-turbidites of modest size in several inland lakes between 39.2°S and 39.8°S, that is, 160–230 km north of the inferred CE 1837 rupture area (Moernaut et al., 2014). The sedimentary record at Chaihuín does not include the CE 1837 tsunami (see discussion in Section 5.4.3), making Gemela West the third site in South-Central Chile with sedimentary evidence for the CE 1837 tsunami and the first one located outside of the presumed rupture area. Alternatively, the G3 deposit could be linked to the CE 1835 earthquake that occurred further north in the Concepción area (36.8°S). However, as the extent of shaking and tsunami inundation was smaller than for the other Concepción events in CE 1751 and CE 2010 (Figure 1; Udías et al., 2012), and shaking strength in Valdivia was much less than in CE 1837 (Lomnitz, 1970), we consider this scenario less likely. As the CE 1837 event produced a transpacific tsunami reported as far as Japan and as far north as Concepción along the Chilean coast (36.8°S; Cisternas et al., 2017), we consider this the best candidate for the G3 deposit.

G2 (CE 1937–1965) is attributed with very high confidence to the CE 1960 megathrust earthquake (M_w 9.5), given the accurate age control (^{137}Cs peak, see Section 5.2)

20554877, 2025, 5, Downloaded from https://onlinelibrary.wiley.com/doi/10.1002/dep2.70031, Wiley Online Library on [16/12/2025]. See the Terms and Conditions (https://onlinelibrary.wiley.com/terms-and-conditions) on Wiley Online Library for rules of use; OA articles are governed by the applicable Creative Commons License

and outstanding size of this tsunami. At the deep basin site, G2 is the thickest tsunami deposit and contains a relatively large amount of remobilised muddy lake sediments (see discussion Section 5.4.2). The G2 deposit adds another data point to the abundant historical and sedimentary evidence for tsunami inundation in CE 1960, which is argued to have been particularly large compared to most previous megathrust earthquake tsunamis (Matos-Llavona et al., 2022).

G1 (2004–2016) is the topmost s1 deposit and can be linked to the CE 2010 Maule earthquake (M_w 8.8). Tsunami run-up of ~2–2.5 m a.s.l. was documented in Niebla (39.9°S; Vargas et al., 2010) and the nearby tide gauge in Corral (39.9°S) shows a maximum sea-level height of 1.6 m a.s.l. (Figure 10A). Although these values might initially seem too small compared to the lake's elevation of 5–6 m a.s.l., they are not direct indicators of the tsunami's maximum vertical reach for two key reasons: First, run-up values measured onshore are typically about three times as large as those recorded in tide gauges (see Figure 1) (Satake, 1994). Second, tsunami wave amplification strongly depends on local submarine and coastal geomorphology, leading to a significant variability in run-up between nearby sites. This is exemplified by the run-up distribution for the 2010 tsunami (Fritz et al., 2011). Thus, despite the CE 2010 rupture ending ~190 km north of our study site, the age of G1 suggests its tsunami may have inundated the lake.

Remarkably, macroscopic observations, CT density and grain-size data for G1 show two sandy pulses, which are separated by muddy organic sediments and an erosional contact. Settling of low-density organic-rich mud would only occur in stable lake conditions after ceasing of tsunami-induced currents, back-wash flow and possible back-and-forth sloshing (seiching) of the lake water (Sabatier et al., 2022). Therefore, we consider it very unlikely that the youngest sand pulse can be attributed to inundation from a later wave during the CE 2010 wave train. Interestingly, the comparable sea-level elevations recorded at Corral during the 2010 Chile tsunami (Figure 10A) and the 2011 Japan tsunami (Figure 10B) suggest that the latter may have induced the upper G1 pulse. If true, this would represent the first deposit in Chile attributed to a remote tsunami.

5.4 | Implications for palaeoseismology and palaeotsunami research in South-Central Chile

5.4.1 | Recurrence of tsunami inundation

Seismo-turbidites in inland lakes and coastal records of subsidence/tsunami inundation show that giant CE 1960-like earthquakes and tsunamis occur on average every three centuries (285 year: Cisternas et al., 2005; 292 year: Moernaut et al., 2018; 325 year: Kempf et al., 2019; 321 year: Wils et al., 2020). The identification of a tsunami deposit for the CE 1737 earthquake in Chaihuín shows that tsunami inundation in this region has occurred more frequently than previously thought, that is, on average every 193 years when considering the last three historical events (CE 1575, 1737 and 1960; Hocking et al., 2021). For tsunamis that were generated by megathrust events along the Chilean subduction zone, the Gemela West record adds the CE 1837 and CE 2010 events to this sequence, leading to a tsunami inundation rate of 109 years at the site, including large tsunamis (CE 1960, 1575) and moderate-size tsunamis (CE 2010, 1837, 1737) at the site. Knowledge of such (relatively) high rates is important for updating tsunami hazard assessment in the CE 1960 rupture area and potentially elsewhere. In order to acquire a complete picture of tsunami inundation hazard, one should also consider rare tele-tsunamis, exemplified by the CE 2011 Japan event. This implies a historical average tsunami inundation rate of 87 years at Gemela West. However, such recurrence value should be treated with caution as the sedimentary evidence is rather ambiguous for the CE 2011 event and it remains unclear how often such tele-tsunamis from Japan or elsewhere would produce notable inundations at the South-Central Chilean coast.

5.4.2 | Changing sensitivity to record tsunami inundation

For adequate tsunami hazard assessment to be successful, palaeotsunami research needs not only to determine how often tsunamis occur but also how large these tsunamis were. Quantifying tsunami flow characteristics from tsunami deposit data (e.g. grain-size) is complex, but forms a growing research field for coastal plain sites (Goff et al., 2012; Masuda et al., 2022; Mitra et al., 2020; Sugawara et al., 2014). Unfortunately, to date, modelling studies for tsunami inundation and sediment transport in coastal lakes are lacking and any inferences are only of first-order relative nature. In Laguna Gemela West, thick and extensive s1 deposits are associated with the largest documented tsunamis, triggered by the CE 1960 and 1575 events, whereas modestly sized s1 deposits are linked to the small local tsunami in CE 1737 and the CE 1837 tsunami produced by a more distant rupture. However, such relationships between deposit size and tsunami size seem to fail for the topmost part of the record where rather large s1 deposits were attributed to the CE 2010 and 2011 tsunamis that were of modest size at our study site. This may suggest a changing sensitivity of the lake to record

20554877, 2025, 5, Downloaded from https://onlinelibrary.wiley.com/doi/10.1002/dep2.70031, Wiley Online Library on [16/12/2025]. See the Terms and Conditions (https://onlinelibrary.wiley.com/terms-and-conditions) on Wiley Online Library for rules of use; OA articles are governed by the applicable Creative Commons License

tsunami deposits as distinctive sand layers. Mechanisms that can have increased that sensitivity are the following:

1. Coseismic subsidence in CE 1960 (documented). An estimated 0.5–0.7 m of coseismic subsidence is documented by Plafker and Savage (1970) for sites close to our study site. About 0.9 m of coseismic subsidence for our site area is proposed based on the inversion model of Ho et al. (2019) which is constructed on the field observations of Plafker and Savage (1970) in combination with nearby and far-field tsunami data. Coseismic subsidence would reduce the width of the beach and lower the barrier made by the Pleistocene sandstone, facilitating tsunami inundations since then. However, as the barrier is currently at ~4.4 m a.s.l., the relative decrease in barrier height is rather modest (10%–16%) and it may have been partly compensated by interseismic uplift because the plate boundary in the study region is highly locked (Moreno et al., 2011). Therefore, we consider the tectonically driven influence on the sensitivity to record tsunamis in this lake to be rather small.
2. Dune migration (documented). As the prevalent wind direction is SW, dune migration can progressively narrow and partially fill the outflow channel (see Figure 2, picture 8). This process could on the one hand somewhat hamper tsunami inflow towards the lake, but on the other hand provide a large source of loose sandy sediments that can be efficiently transported by tsunamis into the lake, given the relatively short distance between the dune blocking and lake (~100 m). So, in case tsunami inflow manages to reach the lake, the resulting lacustrine tsunami deposit would be more prominent in terms of sand content and sand extent. The validity of this mechanism is supported by the overall upward coarsening trend in core Gem01 (c) for both the background sedimentation and the tsunami deposits. Especially since CE 1960, sand content rises to around 30%–40%, whereas this was only 10%–20% in the preceding two to three centuries (Figure 6). This evolution is in accordance with the aerial imagery that shows a vegetated southern lakeshore in CE 1943, which got progressively covered by dune sand forming a 115 m long sandy beach by CE 2023 (Figure 3, Section 4.1).
3. Tsunami erosion of the outlet channel (possible). The largest thickness and highest content of remobilised muddy lake sediment in the CE 1960 deposit in the deep basin suggest a relatively strong erosive power of this tsunami as it entered Laguna Gemela West. Tsunami erosion may also have deepened and widened the channel at the barrier. As the tsunami height in CE 1960 outsized the other events after CE 1575 (see Section 5.3), it is possible that it may have abruptly and permanently increased connectivity for tsunami inundation into Gemela West.

In conclusion, several documented and suggested mechanisms may have increased the sensitivity to record tsunami inundation since the CE 1960 event. This could explain the imprint of the CE 2010 and CE 2011 tsunamis in this lake, even though tsunami size at this coast was relatively small. For other coastal lakes in South-Central Chile, sensitivity changes for palaeotsunami records have been extensively discussed, but seem to be mainly related to tectonically driven changes in relative sea level and associated tidal connectivity to the ocean (Kempf et al., 2020). For example, Lake Budi (38.9°S) shows—in addition to a CE 1960 deposit—only one period 6.4–4.6 kyr BP for which the tsunami deposit record may be complete, whereas tsunami sands from other periods may have been eroded due to tidal currents and tsunami backwash (Wallner, 2007). In contrast, regional correlation of palaeoseismic sites shows that lake Huelde (42.6° S) forms a continuous 5.5 kyr record with up to 17 tsunami deposits. It is interpreted that modest tidal currents may have entered the lake during some periods (Hocking et al., 2025; Kempf et al., 2017). Lake Cucao (42.6° S) has an intermediate record quality because strong tidal currents entered the lake during several periods (e.g. since CE 1960), leading to erosion and bypassing (non-deposition) at several ocean-proximal sites and thus affecting the otherwise continuous 4.3 kyr long tsunami record (Kempf et al., 2020). These differences underscore that—even within a single climatic and overall tectonic setting—several local geomorphological factors (e.g. basin morphology, barrier and channel characteristics, coseismic and interseismic coastal elevation changes, etc.) determine the potential of a coastal lake for palaeotsunami research and that this potential can significantly change over time. Therefore, a specific limnogeological approach and interpretation logic is required for the study of event deposits in each coastal lake system (Sabatier et al., 2022) and quantitative constraints on palaeo-event size require a regional correlation of sedimentary records to reduce record bias due to local geomorphological processes. One of the strengths of Laguna Gemela West is that it is (currently) located well above (5–6 m a.s.l.) the inundation level that is reached by spring tide, meteotsunamis, storms and their combination, but can still be inundated by earthquake-triggered tsunami events. Unlike the lower lying Lake Huelde and Cucao (Kempf et al., 2017, 2020), relative sea-level changes in the order of 1–2 m during giant megathrust earthquakes and post-/inter-seismic periods would not bring the Gemelas system in the tidal range, and thus would not affect tsunami deposit preservation. The setting of Laguna Gemela West is rather similar to Bradley Lake in Cascadia, which

20554877, 2025, 5, Downloaded from https://onlinelibrary.wiley.com/doi/10.1002/dep2.70031, Wiley Online Library on [16/12/2025]. See the Terms and Conditions (https://onlinelibrary.wiley.com/terms-and-conditions) on Wiley Online Library for rules of use; OA articles are governed by the applicable Creative Commons License

is currently located at 5.5 m a.s.l. and at 300–500 m from the ocean (Kelsey et al., 2005). It is renowned as one of the longest (4.6 kyr) continuous palaeotsunami records and was instrumental in reconstructing megathrust earthquake scenarios for the Cascadia subduction zone (Walton et al., 2021). These setting similarities highlight the potential of Laguna Gemela West for extracting a unique Late Holocene palaeotsunami record that is little affected by relative sea-level changes. Extending the record into the Middle Holocene seems more complex as relative sea level in South-Central Chile culminated to 4 ± 2 m above the present level around 6–7 kyr BP (Garrett et al., 2020), and thus, the Gemela West lake system may have been in reach of tidal inflow or storms, and thus, different sedimentary patterns can be expected.

5.4.3 | Complementary value of coastal lakes for palaeotsunami research

The Gemela West record reveals an average recurrence interval of 87 years for tsunami inundation over the past 500 years. This value increases to 109 years when excluding the 2011 Japan tsunami, that is, only considering inundation related to megathrust earthquakes that ruptured less than a few 100 km away. This value is remarkably close to tsunami deposit recurrence (~135 years) in the 1000 year long Cocotué record on the NW coast of Chiloé Island (41.9°S; Cisternas et al., 2018) and the shorter mode (115 years) of the bimodal tsunami recurrence pattern inferred from the 5500 year long Lake Huelde record (42.6°S; Kempf et al., 2019). This contrasts with the longer and unimodal recurrence distribution centred around 292 and 271 years for giant 1960-like earthquakes obtained from the 3500 year palaeoseismic record of Lake Calafquén (Moernaut et al., 2018) and numerical modelling of the megathrust seismic cycle (Julve et al., 2024), respectively. The inference that Laguna Gemela West has recorded a presumably small local tsunami (CE 1737) and two tsunamis that were produced by rupture of adjacent sections (CE 1837 and CE 2010) but not at the site itself, provides a mechanism for the shorter recurrence rate identified in palaeotsunami records. Indeed, partial ruptures both along strike and dip in the CE 1960 rupture area did not produce sufficiently strong and long-duration shaking to produce large turbidity currents that reached the long coring site (CAL1) in Lago Calafquén. However, on more sensitive sites such as RIN2 in Lake Riñihue, seismo-turbidite records do show evidence for ruptures in CE 1737 and CE 1837. Hence, the median recurrence of 126 years in RIN2 is shorter and close to that of Gemela West (109 years) and the short mode in Lake Huelde (115 years). This implies that tsunami records in coastal lakes cannot only provide a complete picture on tsunami inundation hazard at a site (see Section 5.4.1) but can also provide insights into the occurrence and tsunamigenic character of smaller ruptures at the site (e.g. CE 1737) in addition to larger ruptures on adjacent sections (e.g. CE 1837, CE 2010). A similar interpretation was proposed for explaining periods of relatively high-frequency tsunami inundation in the Bradley Lake palaeotsunami record (Kelsey et al., 2005) when compared to coastal plain/marsh sites along the Cascadia Margin. In contrast to coastal lakes and coastal marshes in a ridge-and-swale topography (Jankaew et al., 2008; Monecke et al., 2008), many sites on coastal plains and marshes may only record tsunami inundation when coseismic subsidence creates sufficient accommodation space to preserve the tsunami deposit. This is exemplified by the absence of a CE 2010 and CE 1837 tsunami deposit at the nearby Chaihuín site (Figure 8; Hocking et al., 2021) and the absence of the CE 1837 tsunami deposit at the Maullín site (Cisternas et al., 2005). These events did not produce coseismic coastal subsidence at these sites. Especially the absence of a CE 1837 tsunami deposit in Maullín points to a lack of preservation potential as it can be expected that this large (trans-Pacific) tsunami inundated the site located at the northern edge of the presumed rupture area. In turn, an advantage of coastal plains/marshes over coastal lakes is that coastal elevation changes can be identified and quantified by transfer function models applied on diatom stratigraphy, thus providing insights into the megathrust rupture location, depth and slip values (Dura et al., 2016; Hocking et al., 2017).

6 | CONCLUSIONS

Our sedimentological and geochemical analysis of the sedimentary infill of Laguna Gemela West shows that it contains a record with high temporal resolution of tsunamis that affected the region over the last 500 years. It is suggested that only long-period tsunami waves with sufficient height are capable of inundating the lake at 5–6 m a.s.l. through the 400 m long winding channel. Good age control allows us to support the recent notion, based on a coastal marsh record (Chaihuín site), that the local megathrust earthquake of CE 1737 was tsunamigenic. Laguna Gemela West forms a sensitivity recorder of tsunami inundation in which modestly sized tsunamis also left an imprint, such as those caused by the small local rupture of CE 1737 and the large ruptures of adjoining megathrust sections in CE 1837 and CE 2010, located >100 and 190 km south and north from Gemela West, respectively. Moreover, inundation by the CE 2011 Japan tele-tsunami is potentially recorded.

20554877, 2025, 5, Downloaded from https://onlinelibrary.wiley.com/doi/10.1002/dep2.70031, Wiley Online Library on [16/12/2025]. See the Terms and Conditions (https://onlinelibrary.wiley.com/terms-and-conditions) on Wiley Online Library for rules of use; OA articles are governed by the applicable Creative Commons License

These results imply that Laguna Gemela West—and coastal lakes in general—can reveal relatively short tsunami recurrence rates, providing a more complete picture on local tsunami inundation hazard than many coastal plain/marsh sites, which often require coseismic subsidence to provide sufficient accommodation space for tsunami deposits to be preserved. Compared to coastal plains/marshes and low-lying coastal lakes, the effect of relative sea-level change may be less influential on the record length and record quality in Gemela West, but local geomorphological dynamics related to dune migration and channel erosion may have changed the sensitivity for recording tsunami inundations. This study shows the high potential of Laguna Gemela West to contain a Late Holocene palaeotsunami record that can provide information complementary to the existing regional palaeoseismic and palaeotsunami data, enabling us to better understand the megathrust earthquake cycle in South-Central Chile by constraining past megathrust earthquake scenarios in terms of timing, location and rupture depth.

ACKNOWLEDGEMENTS

We dedicate this paper to Judy McKenzie. Her efforts to support and promote limnogeological research at ETH Zurich helped to transform the entire discipline, by conceptually considering lakes as 'small analogs for oceans' and as 'natural laboratories' to investigate a broad spectrum of geological, geochemical and sedimentological processes. This research was supported by internal funding of RCMG, Fondecyt project no. 1150346 and FWO-Vlaanderen. This research was funded in whole or in part by the Austrian Science Fund (FWF) [10.55776/P30285]. For open access purposes, the author has applied a CC BY public copyright licence to any author accepted manuscript version arising from this submission. Matías Carvajal acknowledges the support of Chile's Fondo Nacional de Desarrollo Científico y Tecnológico, FONDECYT Project 1231735. We thank R. Brummer and A. Abarzúa (UACh) for fieldwork equipment. Our gratitude goes to K. De Rycker for invaluable technical support. The Nature Conservancy is acknowledged for granting us permission to conduct our research within the Valdivian Coastal Reserve. R. Achten is acknowledged for giving access to the CT scanner of the Ghent University Hospital. Geochemical data were acquired at the XRF Core Scanning Lab at MARUM in Bremen, for which we thank U. Röhl and V. Lukies. We thank Marcel Ortler (Univ. Innsbruck) for the Python scripts regarding XRF data analysis. Our gratitude goes to Katrin Monecke and an anonymous reviewer for constructive reviews of an earlier version of this manuscript. N/A

CONFLICT OF INTEREST STATEMENT

The authors declare no conflict of interest.

DATA AVAILABILITY STATEMENT

The data that support the findings of this study are available from the corresponding author upon reasonable request.

ORCID

Markus Niederstätter https://orcid.org/0009-0009-9137-588X
Marc De Batist https://orcid.org/0000-0002-1625-2080

REFERENCES

Abe, K. (1979) Size of great earthquakes of 1837–1974 inferred from tsunami data. *Journal of Geophysical Research*, 84, 1561–1568. Available from: https://doi.org/10.1029/jb084ib04p01561

Alaniz, A.J., Abarzúa, A.M., Martel-Cea, A., Jarpa, L., Hernández, M., Aquino-López, M.A. & Smith-Ramírez, C. (2021) Linking sedimentological and spatial analysis to assess the impact of the forestry industry on soil loss: the case of Lanalhue Basin, Chile. *Catena*, 207, 105660. Available from: https://doi.org/10.1016/j.catena.2021.105660

Arnaud, F., Magand, O., Chapron, E., Bertrand, S., Boës, X., Charlet, F. & Mélières, M.A. (2006) Radionuclide dating (^{210}Pb, ^{137}Cs, ^{241}Am) of recent lake sediments in a highly active geodynamic setting (Lakes Puyehue and Icalma-Chilean Lake District). *Science of the Total Environment*, 366, 837–850. Available from: https://doi.org/10.1016/j.scitotenv.2005.08.013

Avşar, U. (2019) Sedimentary geochemical evidence of historical tsunamis in the Eastern Mediterranean from Ölüdeniz Lagoon, SW Turkey. *Journal of Paleolimnology*, 61, 373–385. Available from: https://doi.org/10.1007/s10933-018-00065-x

Blaauw, M. & Christen, J.A. (2011) Flexible paleoclimate age-depth models using an autoregressive gamma process. *Bayesian Analysis*, 6, 457–474. Available from: https://doi.org/10.1214/11-BA618

Blott, S.J. & Pye, K. (2001) GRADISTAT: a grain size distribution and statistics package for the analysis of unconsolidated sediments. *Earth Surface Processes and Landforms*, 26, 1237–1248. Available from: https://doi.org/10.1002/esp.261

Boak, E.H. & Turner, I.L. (2005) Shoreline definition and detection: a review. *Journal of Coastal Research*, 21, 688–703. Available from: https://doi.org/10.2112/03-0071.1

Bondevik, S., Svendsen, J.I. & Mangerud, J. (1997) Tsunami sedimentary facies deposited by the Storegga tsunami in shallow marine basins and coastal lakes, western Norway. *Sedimentology*, 44, 1115–1131. Available from: https://doi.org/10.1046/J.1365-3091.1997.D01-63.X

Carvajal, M., Cisternas, M. & Catalán, P.A. (2017) Source of the 1730 Chilean earthquake from historical records: implications for the future tsunami hazard on the coast of Metropolitan Chile. *Journal of Geophysical Research: Solid Earth*, 122, 3648–3660. Available from: https://doi.org/10.1002/2017JB014063

Carvajal, M., Contreras-López, M., Winckler, P. & Sepúlveda, I. (2017) Meteotsunamis occurring along the Southwest Coast of South America during an intense storm. *Pure and Applied*

20554877, 2025, 5, Downloaded from https://onlinelibrary.wiley.com/doi/10.1002/dep2.70031, Wiley Online Library on [16/12/2025]. See the Terms and Conditions (https://onlinelibrary.wiley.com/terms-and-conditions) on Wiley Online Library for rules of use; OA articles are governed by the applicable Creative Commons License

Geophysics, 174, 3313–3323. Available from: https://doi.org/10.1007/s00024-017-1584-0

Chagué-Goff, C., Szczuciński, W. & Shinozaki, T. (2017) Applications of geochemistry in tsunami research: a review. *Earth-Science Reviews*, 165, 203–244. Available from: https://doi.org/10.1016/j.earscirev.2016.12.003

Cisternas, M., Atwater, B.F., Torrejón, F., Sawai, Y., Machuca, G., Lagos, M., Eipert, A., Youlton, C., Salgado, I., Kamataki, T., Shishikura, M., Rajendran, C.P., Malik, J.K., Rizal, Y. & Husni, M. (2005) Predecessors of the giant 1960 Chile earthquake. *Nature*, 437, 404–407. Available from: https://doi.org/10.1038/nature03943

Cisternas, M., Carvajal, M., Wesson, R., Ely, L.L. & Gorigoitia, N. (2017) Exploring the historical earthquakes preceding the giant 1960 Chile earthquake in a time-dependent seismogenic zone. *Bulletin of the Seismological Society of America*, 107, 2664–2675. Available from: https://doi.org/10.1785/0120170103

Cisternas, M., Garrett, E., Wesson, R., Dura, T. & Ely, L.L. (2018) Unusual geologic evidence of coeval seismic shaking and tsunamis shows variability in earthquake size and recurrence in the area of the giant 1960 Chile earthquake. *Marine Geology*, 396, 54–66. Available from: https://doi.org/10.1016/j.margeo.2018.01.005

Clark, K., Howarth, J., Litchfield, N., Cochran, U., Turnbull, J., Dowling, L., Howell, A., Berryman, K. & Wolfe, F. (2019) Geological evidence for past large earthquakes and tsunamis along the Hikurangi subduction margin, New Zealand. *Marine Geology*, 412, 139–172. Available from: https://doi.org/10.1016/j.margeo.2019.03.004

Di Castri, F. & Hajek, E.R. (1976) *Bioclimatología de Chile*. Santiago: Vicerrectoría Académica de la Universidad Católica de Chile.

Dura, T., Hemphill-Haley, E., Sawai, Y. & Horton, B.P. (2016) The application of diatoms to reconstruct the history of subduction zone earthquakes and tsunamis. *Earth-Science Reviews*, 152, 181–197. Available from: https://doi.org/10.1016/j.earscirev.2015.11.017

Dura, T., Horton, B.P., Cisternas, M., Ely, L.L., Hong, I., Nelson, A.R., Wesson, R.L., Pilarczyk, J.E., Parnell, A.C. & Nikitina, D. (2017) Subduction zone slip variability during the last millennium, south-central Chile. *Quaternary Science Reviews*, 175, 112–137. Available from: https://doi.org/10.1016/j.quascirev.2017.08.023

Egbert, G.D. & Erofeeva, S.Y. (2002) Efficient inverse modeling of barotropic ocean tides. *Journal of Atmospheric and Oceanic Technology*, 19, 183–204. Available from: https://doi.org/10.1175/1520-0426(2002)019<0183:EIMOBO>2.0.CO;2

Ely, L.L., Cisternas, M., Wesson, R.L. & Dura, T. (2014) Five centuries of tsunamis and land-level changes in the overlapping rupture area of the 1960 and 2010 Chilean earthquakes. *Geology*, 42, 995–998. Available from: https://doi.org/10.1130/G35830.1

Flanders Marine Institute (VLIZ). (2024) Intergovernmental Oceanographic Commission (IOC) (2024): sea level station monitoring facility. Available from: https://doi.org/10.14284/482; https://www.ioc-sealevelmonitoring.org/

Fritz, H.M., Petroff, C.M., Catalán, P.A., Cienfuegos, R., Winckler, P., Kalligeris, N., Weiss, R., Barrientos, S.E., Meneses, G., Valderas-Bermejo, C., Ebeling, C., Papadopoulos, A., Contreras, M., Almar, R., Dominguez, J.C. & Synolakis, C.E. (2011) Field Survey of the 27 February 2010 Chile Tsunami. *Pure and Applied Geophysics*, 168, 1989–2010. Available from: https://doi.org/10.1007/s00024-011-0283-5

Garrett, E., Melnick, D., Dura, T., Cisternas, M., Ely, L.L., Wesson, R.L., Jara-Muñoz, J. & Whitehouse, P.L. (2020) Holocene relative sea-level change along the tectonically active Chilean coast. *Quaternary Science Reviews*, 236, 106281. Available from: https://doi.org/10.1016/j.quascirev.2020.106281

Garrett, E., Shennan, I., Woodroffe, S.A., Cisternas, M., Hocking, E.P. & Gulliver, P. (2015) Reconstructing paleoseismic deformation, 2: 1000 years of great earthquakes at Chucalén, south central Chile. *Quaternary Science Reviews*, 113, 112–122. Available from: https://doi.org/10.1016/j.quascirev.2014.10.010

Goff, J., Chagué-Goff, C., Nichol, S., Jaffe, B. & Dominey-Howes, D. (2012) Progress in palaeotsunami research. *Sedimentary Geology*, 243, 70–88. Available from: https://doi.org/10.1016/j.sedgeo.2011.11.002

Ho, T.C., Satake, K., Watada, S. & Fujii, Y. (2019) Source Estimate for the 1960 Chile Earthquake from joint inversion of geodetic and transoceanic tsunami data. *Journal of Geophysical Research: Solid Earth*, 124, 2812–2828. Available from: https://doi.org/10.1029/2018JB016996

Hocking, E.P., Garrett, E., Aedo, D., Carvajal, M. & Melnick, D. (2021) Geological evidence of an unreported historical Chilean tsunami reveals more frequent inundation. *Communications Earth & Environment*, 2, 245. Available from: https://doi.org/10.1038/s43247-021-00319-z

Hocking, E.P., Garrett, E. & Cisternas, M. (2017) Modern diatom assemblages from Chilean tidal marshes and their application for quantifying deformation during past great earthquakes. *Journal of Quaternary Science*, 32, 396–415. Available from: https://doi.org/10.1002/jqs.2933

Hocking, E.P., Kempf, P., Pleskot, K., Suchora, M., Kołaczek, P., Niederstätter, M. & Moernaut, J. (2025) Environmental response of coastal lake Huelde, Chile, after tsunami inundation and earthquake-induced subsidence. *Quaternary Science Reviews*, 365, 109474. Available from: https://doi.org/10.1016/J.QUASCIREV.2025.109474

Hogg, A.G., Heaton, T.J., Hua, Q., Palmer, J.G., Turney, C.S.M., Southon, J., Bayliss, A., Blackwell, P.G., Boswijk, G., Bronk Ramsey, C., Pearson, C., Petchey, F., Reimer, P., Reimer, R. & Wacker, L. (2020) SHCal20 southern hemisphere calibration, 0–55,000 years cal BP. *Radiocarbon*, 62, 759–778. Available from: https://doi.org/10.1017/RDC.2020.59

Hu, G., Li, L., Ren, Z. & Zhang, K. (2023) The characteristics of the 2022 Tonga volcanic tsunami in the Pacific Ocean. *Natural Hazards and Earth System Sciences*, 23, 675–691. Available from: https://doi.org/10.5194/NHESS-23-675-2023

Illies, H. (1970) *Geología de los alrededores de Valdivia y Volcanismo y Tectónica en márgenes del Pacífico en Chile meridional*. Valdivia (Chile): Universidad Austral de Chile.

Jackson, K.L., Eberli, G.P., Amelung, F., McFadden, M.A., Moore, A.L., Rankey, E.C. & Jayasena, H.A.H. (2014) Holocene Indian Ocean tsunami history in Sri Lanka. *Geology*, 42, 859–862. Available from: https://doi.org/10.1130/G35796.1

Jankaew, K., Atwater, B.F., Sawai, Y., Choowong, M., Charoentitirat, T., Martin, M.E. & Prendergast, A. (2008) Medieval forewarning of the 2004 Indian Ocean tsunami in Thailand. *Nature*, 455, 1228–1231. Available from: https://doi.org/10.1038/nature07373

Jarrin, P., Nocquet, J.M., Rolandone, F., Mora-Páez, H., Mothes, P. & Cisneros, D. (2022) Current motion and deformation of the Nazca Plate: new constraints from GPS measurements.

20554877, 2025, 5, Downloaded from https://onlinelibrary.wiley.com/doi/10.1002/dep2.70031, Wiley Online Library on [16/12/2025]. See the Terms and Conditions (https://onlinelibrary.wiley.com/terms-and-conditions) on Wiley Online Library for rules of use; OA articles are governed by the applicable Creative Commons License

Geophysical Journal International, 232, 842–863. Available from: https://doi.org/10.1093/GJI/GGAC353

Joe-Wong, C., Schlesinger, D.R., Chow, A.T. & Myneni, S.C.B. (2019) Sea level rise produces abundant organobromines in salt-affected coastal wetlands. *Geochemical Perspectives Letters*, 10, 31–35. Available from: https://doi.org/10.7185/geochemlet.1911

Julve, J., Barbot, S., Moreno, M., Tassara, A., Araya, R., Catalán, N., Crempien, J.G.F. & Becerra-Carreño, V. (2024) Recurrence time and size of Chilean earthquakes influenced by geological structure. *Nature Geoscience*, 17, 79–87. Available from: https://doi.org/10.1038/s41561-023-01327-8

Kelsey, H.M., Nelson, A.R., Hemphill-Haley, E. & Witter, R.C. (2005) Tsunami history of an Oregon coastal lake reveals a 4600 yr record of great earthquakes on the Cascadia subduction zone. *Geological Society of America Bulletin*, 117, 1009. Available from: https://doi.org/10.1130/B25452.1

Kempf, P., Moernaut, J. & De Batist, M. (2019) Bimodal recurrence pattern of tsunamis in South-Central Chile: a statistical exploration of paleotsunami data. *Seismological Research Letters*, 90, 194–202. Available from: https://doi.org/10.1785/0220180204

Kempf, P., Moernaut, J., Van Daele, M., Pino, M., Urrutia, R. & De Batist, M. (2020) Paleotsunami record of the past 4300 years in the complex coastal lake system of Lake Cucao, Chiloé Island, south central Chile. *Sedimentary Geology*, 401, 105644. Available from: https://doi.org/10.1016/j.sedgeo.2020.105644

Kempf, P., Moernaut, J., Van Daele, M., Vandoorne, W., Pino, M., Urrutia, R. & De Batist, M. (2017) Coastal lake sediments reveal 5500 years of tsunami history in south central Chile. *Quaternary Science Reviews*, 161, 99–116. Available from: https://doi.org/10.1016/j.quascirev.2017.02.018

Kempf, P., Moernaut, J., Van Daele, M., Vermassen, F., Vandoorne, W., Pino, M., Urrutía, R., Schmidt, S., Garrett, E. & De Batist, M. (2015) The sedimentary record of the 1960 tsunami in two coastal lakes on Isla de Chiloé, south central Chile. *Sedimentary Geology*, 328, 73–86. Available from: https://doi.org/10.1016/j.sedgeo.2015.08.004

Koutsodendris, A., Brauer, A., Friedrich, O., Tjallingii, R., Putyrskaya, V., Hennrich, B., Kühn, R., Klemt, E. & Pross, J. (2023) Natural and human-induced ecosystem change in SE Europe since AD 1700 derived from a partially varved sediment record from Lake Vouliagmeni (Greece). *The Holocene*, 33, 1207–1220. Available from: https://doi.org/10.1177/09596836231183062

Lagos, R. (2008) Sobre el origen de los lagos gemelos de Colún, Valdivia, Chile. *Espacio Regional*, 2, 13–25.

León, T., Lau, A.Y.A., Easton, G. & Goff, J. (2023) A comprehensive review of tsunami and palaeotsunami research in Chile. *Earth-Science Reviews*, 236, 104273. Available from: https://doi.org/10.1016/j.earscirev.2022.104273

Lomnitz, C. (1970) Major earthquakes and tsunamis in Chile during the period 1535 to 1955. *Geologische Rundschau*, 59(59), 938–960. Available from: https://doi.org/10.1007/BF02042278

Lomnitz, C. (2004) Major earthquakes of Chile: a historical survey, 1535-1960. *Seismological Research Letters*, 75, 368–378. Available from: https://doi.org/10.1785/gssrl.75.3.368

Lundine, M. (2018) Optimizing UAV surveys for coastal morphodynamics: estimation of spatial uncertainty as a function of flight acquisition and post-processing factors. Augustana College.

Lynett, P., McCann, M., Zhou, Z., Renteria, W., Borrero, J., Greer, D., Fa'anunu, O., Bosserelle, C., Jaffe, B., La Selle, S., Ritchie, A., Snyder, A., Nasr, B., Bott, J., Graehl, N., Synolakis, C., Ebrahimi, B. & Cinar, G.E. (2022) Diverse tsunamigenesis triggered by the Hunga Tonga-Hunga Ha'apai eruption. *Nature*, 609, 728–733. Available from: https://doi.org/10.1038/s41586-022-05170-6

Masuda, H., Sugawara, D., Abe, T. & Goto, K. (2022) To what extent tsunami source information can be extracted from tsunami deposits? Implications from the 2011 Tohoku-oki tsunami deposits and sediment transport simulations. *Progress in Earth and Planetary Science*, 9, 65. Available from: https://doi.org/10.1186/s40645-022-00527-x

Matos-Llavona, P.I., Ely, L.L., MacInnes, B., Dura, T., Cisternas, M.A., Bourgeois, J., Bruce, D., DePaolis, J., Dolcimascolo, A., Horton, B.P., Melnick, D., Nelson, A.R., Szeliga, W. & Wesson, R.L. (2022) The giant 1960 tsunami in the context of a 6000-year record of paleotsunamis and coastal evolution in south-central Chile. *Earth Surface Processes and Landforms*, 47, 2062–2078. Available from: https://doi.org/10.1002/esp.5363

Meteoblue. (2025) Visualization based on ERA5 reanalysis data. Available from: https://www.meteoblue.com/en/climate-change/valdivia_chile_3868707?month=6 [Accessed 28 June 2025].

Mitra, R., Naruse, H. & Abe, T. (2020) Estimation of tsunami characteristics from deposits: inverse modeling using a deep-learning neural network. *Journal of Geophysical Research: Earth Surface*, 125, e2020JF005583. Available from: https://doi.org/10.1029/2020JF005583

Moernaut, J., Van Daele, M., Fontijn, K., Heirman, K., Kempf, P., Pino, M., Valdebenito, G., Urrutia, R., Strasser, M. & De Batist, M. (2018) Larger earthquakes recur more periodically: new insights in the megathrust earthquake cycle from lacustrine turbidite records in south-central Chile. *Earth and Planetary Science Letters*, 481, 9–19. Available from: https://doi.org/10.1016/j.epsl.2017.10.016

Moernaut, J., Van Daele, M., Heirman, K., Fontijn, K., Strasser, M., Pino, M., Urrutia, R. & De Batist, M. (2014) Lacustrine turbidites as a tool for quantitative earthquake reconstruction: new evidence for a variable rupture mode in south central Chile. *Journal of Geophysical Research: Solid Earth*, 119, 1607–1633. Available from: https://doi.org/10.1002/2013JB010738

Monecke, K., Finger, W., Klarer, D., Kongko, W., McAdoo, B.G., Moore, A.L. & Sudrajat, S.U. (2008) A 1,000-year sediment record of tsunami recurrence in northern Sumatra. *Nature*, 455, 1232–1234. Available from: https://doi.org/10.1038/nature07374

Moreno, M., Melnick, D., Rosenau, M., Bolte, J., Klotz, J., Echtler, H., Baez, J., Bataille, K., Chen, J., Bevis, M., Hase, H. & Oncken, O. (2011) Heterogeneous plate locking in the South-Central Chile subduction zone: building up the next great earthquake. *Earth and Planetary Science Letters*, 305, 413–424. Available from: https://doi.org/10.1016/j.epsl.2011.03.025

Moreno, M.S., Bolte, J., Klotz, J. & Melnick, D. (2009) Impact of megathrust geometry on inversion of coseismic slip from geodetic data: application to the 1960 Chile earthquake. *Geophysical Research Letters*, 36, L16310. Available from: https://doi.org/10.1029/2009GL039276

Morton, R.A., Gelfenbaum, G. & Jaffe, B.E. (2007) Physical criteria for distinguishing sandy tsunami and storm deposits using modern examples. *Sedimentary Geology*, 200, 184–207. Available from: https://doi.org/10.1016/j.sedgeo.2007.01.003

20554877, 2025, 5, Downloaded from https://onlinelibrary.wiley.com/doi/10.1002/dep2.70031, Wiley Online Library on [16/12/2025]. See the Terms and Conditions (https://onlinelibrary.wiley.com/terms-and-conditions) on Wiley Online Library for rules of use; OA articles are governed by the applicable Creative Commons License

NOAA; National Geophysical Data Center/World Data Service. (2025) Global Historical Tsunami Database. NOAA National Centers for Environmental Information. Available from: https://doi.org/10.7289/V5PN93H7

Oldfield, F. & Appleby, P.G. (1984) *Empirical testing of 210Pb-dating models for lake sediments*. United Kingdom: Leicester University Press.

Palacios, N. (2008) Caracterización del macrozoobentos en la relación a la profundidad en un lago costero de agua dulce: Región de los Riós (XIV), Chile. Universidad Austral de Chile, MSc Thesis.

Philibosian, B. & Meltzner, A.J. (2020) Segmentation and supercycles: a catalog of earthquake rupture patterns from the Sumatran Sunda Megathrust and other well-studied faults worldwide. *Quaternary Science Reviews*, 241, 106390. Available from: https://doi.org/10.1016/j.quascirev.2020.106390

Pillay, M.T. & Fitchett, J.M. (2021) Southern hemisphere tropical cyclones: a critical analysis of regional characteristics. *International Journal of Climatology*, 41, 146–161. Available from: https://doi.org/10.1002/joc.6613

Plafker, G. & Savage, J.C. (1970) Mechanism of the Chilean earthquakes of May 21 and 22, 1960. *Bulletin of the Geological Society of America*, 81, 1001–1030. Available from: https://doi.org/10.1130/0016-7606(1970)81[1001:MOTCEO]2.0.CO;2

Ruiz, S. & Madariaga, R. (2018) Historical and recent large megathrust earthquakes in Chile. *Tectonophysics*, 733, 37–56. Available from: https://doi.org/10.1016/j.tecto.2018.01.015

Sabatier, P., Moernaut, J., Bertrand, S., Van Daele, M., Kremer, K., Chaumillon, E. & Arnaud, F. (2022) A Review of Event Deposits in Lake Sediments. *Quaternary*, 5, 1–47. Available from: https://doi.org/10.3390/quat5030034

Satake, K. (1994) Mechanism of the 1992 Nicaragua Tsunami Earthquake. *Geophysical Research Letters*, 21, 2519–2522. Available from: https://doi.org/10.1029/94GL02338

Sawai, Y., Fujii, Y., Fujiwara, O., Kamataki, T., Komatsubara, J., Okamura, Y., Satake, K. & Shishikura, M. (2008) Marine incursions of the past 1500 years and evidence of tsunamis at Suijin-numa, a coastal lake facing the Japan Trench. *Holocene*, 18, 517–528. Available from: https://doi.org/10.1177/0959683608089206

SERNAGEOMIN. (2003) Mapa Geológico de Chile: versión digital.

Sugawara, D., Goto, K. & Jaffe, B.E. (2014) Numerical models of tsunami sediment transport—current understanding and future directions. *Marine Geology*, 352, 295–320. Available from: https://doi.org/10.1016/j.margeo.2014.02.007

Udías, A., Madariaga, R., Buforn, E., Muñoz, D. & Ros, M. (2012) The large Chilean historical earthquakes of 1647, 1657, 1730, and 1751 from contemporary documents. *Bulletin of the Seismological Society of America*, 102, 1639–1653. Available from: https://doi.org/10.1785/0120110289

Vargas, G., Farías, M., Carretier, S., Tassara, A., Baize, S. & Melnick, D. (2010) Coastal uplift and tsunami effects associated to the 2010 Mw 8.8 Maule earthquake in Central Chile. *Andean Geology*, 38, 219–238.

Vega, R.M., Mella, M., Nielsen, S.N. & Pino, M. (2018) Stratigraphy and sedimentology of a late Pleistocene incised valley fill: a depositional and paleogeographic model for "Cancagua" deposits in north-western Patagonia, Chile. *Andean Geology*, 45, 161–185. Available from: https://doi.org/10.5027/ANDGEOV45N2-3030

Wallner, J. (2007) Holozäne Landschaftsentwicklung am Lago Budi, Chile (38.9°S)—Paläolimnologisch/paläoseismische Untersuchungen an Lagunensedimenten. Friedrich-Schiller-Universität Jena. PhD Thesis.

Walton, M.A.L., Staisch, L.M., Dura, T., Pearl, J.K., Sherrod, B., Gomberg, J., Engelhart, S., Tréhu, A., Watt, J., Perkins, J., Witter, R.C., Bartlow, N., Goldfinger, C., Kelsey, H., Morey, A.E., Sahakian, V.J., Tobin, H., Wang, K., Wells, R. & Wirth, E. (2021) Toward an integrative geological and geophysical view of Cascadia subduction zone earthquakes. *Annual Review of Earth and Planetary Sciences*, 49, 367–398. Available from: https://doi.org/10.1146/annurev-earth-071620-065605

Ward, J.H. (1963) Hierarchical grouping to optimize an objective function. *Journal of the American Statistical Association*, 58, 236–244. Available from: https://doi.org/10.2307/2282967

Weltje, G.J. & Tjallingii, R. (2008) Calibration of XRF core scanners for quantitative geochemical logging of sediment cores: theory and application. *Earth and Planetary Science Letters*, 274, 423–438. Available from: https://doi.org/10.1016/j.epsl.2008.07.054

Wils, K., Van Daele, M., Kissel, C., Moernaut, J., Schmidt, S., Siani, G. & Lastras, G. (2020) Seismo-turbidites in Aysén Fjord (southern Chile) reveal a complex pattern of rupture modes along the 1960 megathrust earthquake segment. *Journal of Geophysical Research: Solid Earth*, 125, e2020JB019405. Available from: https://doi.org/10.1029/2020JB019405

Winckler, P., Contreras-López, M., Campos-Caba, R., Beyá, J.F., & Molina, M. (2017) El temporal del 8 de agosto de 2015 en las regiones de Valparaíso y Coquimbo, Chile central. *Latin American Journal of Aquatic Research*, 45, 622–648. Available from: https://doi.org/10.3856/vol45-issue4-fulltext-1

Zhang, B., Ding, X., Amelung, F., Wang, C., Xu, W., Zhu, W., Shimada, M., Zhang, Q. & Baba, T. (2021) Impact of ionosphere on InSAR observation and coseismic slip inversion: improved slip model for the 2010 Maule, Chile, earthquake. *Remote Sensing of Environment*, 267, 112733. Available from: https://doi.org/10.1016/j.rse.2021.112733

SUPPORTING INFORMATION

Additional supporting information can be found online in the Supporting Information section at the end of this article.

How to cite this article: Moernaut, J., Boes, E., Melnick, D., Carvajal, M., Niederstätter, M., Schmidt, S. et al. (2025) A continuous 500-year sediment record of inundation by local and distant tsunamis in South-Central Chile (40.1°S). *The Depositional Record*, 11, 1285–1310. Available from: https://doi.org/10.1002/dep2.70031

20554877, 2025, 5, Downloaded from https://onlinelibrary.wiley.com/doi/10.1002/dep2.70031, Wiley Online Library on [16/12/2025]. See the Terms and Conditions (https://onlinelibrary.wiley.com/terms-and-conditions) on Wiley Online Library for rules of use; OA articles are governed by the applicable Creative Commons License